AGU PUBLICATIONS

JGR

Journal of Geophysical Research: Solid Earth

RESEARCH ARTICLE

10.1002/2014JB011430

Key Points:
- Localized areas show higher sensitivity to UDSS than their surroundings
- The majority of LFEs fail during times of positive and increasing UDSS
- RTRs with duration and velocity of 4 h and 5 km/h; high sensitivity to UDSS

Supporting Information:
- Readme
- Text S1
- Figure S1
- Figure S2
- Figure S3
- Figure S4
- Table S1

Correspondence to:
A. A. Royer,
aroyer@eos.ubc.ca

Citation:
Royer, A. A., A. M. Thomas, and M. G. Bostock (2015), Tidal modulation and triggering of low-frequency earthquakes in northern Cascadia, *J. Geophys. Res. Solid Earth*, *120*, doi:10.1002/2014JB011430.

Received 7 JUL 2014
Accepted 19 DEC 2014
Accepted article online 29 DEC 2014

Tidal modulation and triggering of low-frequency earthquakes in northern Cascadia

A. A. Royer[1], A. M. Thomas[2], and M. G. Bostock[1]

[1] Department of Earth, Ocean and Atmospheric Sciences, University of British Columbia, Vancouver, British Columbia, Canada, [2] Department of Geophysics, Stanford University, Stanford, California, USA,

Abstract We analyze the influence of Earth and ocean tides on the triggering of low-frequency earthquakes (LFEs) in northern Cascadia using three LFE catalogs for southern Vancouver Island and Washington state from episodic tremor and slip events between 2003 and 2013. Sensitivities of LFE families to tidally induced fault normal stress, updip shear stress (UDSS), and corresponding time derivatives are computed and their geographic variability is mapped. We find localized areas showing higher sensitivity to UDSS than their surroundings, suggesting that tidal sensitivity depends on laterally heterogeneous physical properties such as variable pore fluid pressures and frictional properties along the plate interface. We observe that sensitivity of LFEs to UDSS rises dramatically from near zero on the first day of strong activity to a maximum ~4 days later. In addition, the peak LFE rate transitions from a correlation with peak tidal shear stress rate to a correlation with peak tidal shear stress through large slow slip events. We identify 64 Rapid-Tremor-Reversals (RTRs) that start a few days after the main slip front. The RTRs have an average stress drop of ~0.8 kPa and a majority (72%) occurs during periods of large positive UDSS. The combined observations imply that RTRs play an important role in slow slip processes and that modulation of creep rate due to tidal stress and tidal triggering of secondary events are jointly responsible for the observed tidal sensitivity.

1. Introduction

It has become increasingly evident in recent years that slow slip, tectonic tremor, and low-frequency earthquakes (LFEs) are sensitive to small stress changes. Perturbations at levels of several tens of kPa, as generated by surface wave trains from teleseismic events, are capable of triggering tremor [*Miyazawa and Mori*, 2005; *Peng and Chao*, 2008; *Peng et al.*, 2008; *Rubinstein et al.*, 2007, 2009], whereas tidal stresses at levels between 1 and 10 kPa have been shown to modulate slip [*Hawthorne and Rubin*, 2010, 2013], tectonic tremor [*Rubinstein et al.*, 2008; *Nakata et al.*, 2008; *Lambert et al.*, 2009; *Thomas et al.*, 2013; *Klaus*, 2012; *Gallego et al.*, 2013; *Ide and Tanaka*, 2014], and LFEs [*Shelly et al.*, 2007a; *Thomas et al.*, 2012] during periods of tremor and associated slip. The analysis of tidal sensitivity, in particular, has led to important insights into the mechanism underlying the slow slip phenomena.

The first report of tidal modulation of tectonic tremor in northern Cascadia was made by *Rubinstein et al.* [2008] who identified clear pulsing of tremor activity with periods of 12.4 and 24 to 25 h, corresponding to the principal lunar (M2) and lunisolar tides. A study of tremor below southern Vancouver Island by *Lambert et al.* [2009] demonstrated that peak tremor activity occurs at times of maximum tidal shear stress in the thrust direction, suggesting that tidal tremor and slip are collocated. Similar modulation of tremor by tidal shear stress has been observed in southwest Japan beneath Shikoku [*Nakata et al.*, 2008; *Ide*, 2010] and northern Washington [*Klaus*, 2012]. To better understand the influence of tidal stresses on slow slip, *Hawthorne and Rubin* [2010] analyzed strainmeter records from northern Washington and southern Vancouver Island for episodic tremor and slip (ETS) events between 2007 and 2009. They observed tidal modulation of slow-slip-induced strain at the 12.4 h M2 period compatible with peak strain rate occurring somewhere between the time of maximum shear stressing rate and maximum shear stress, depending on slip location. *Hawthorne and Rubin* [2013] used a velocity-weakening to velocity-strengthening friction law to model slow slip events (SSEs) in the presence of periodic shear stress to simulate the tides. Their simulations produced quasi-sinusoidal tidal modulation of the slip rate, with the maximum moment rate occurring close to the maximum applied stress. *Houston et al.* [2011] found that during ETS events, tremor occasionally propagates rapidly (at 4 to 13 km/s) in the direction opposing the advancing tremor and slip front in rapid tremor reversals (RTRs). It propagates still more rapidly in streaks in updip and downdip directions near the advancing tremor and slip front [*Shelly et al.*, 2007a; *Ghosh et al.*, 2010]. *Thomas et al.* [2013] noted that large, high-amplitude RTRs and tremor streaks in northern Washington occur almost exclusively during times of positive, thrust-encouraging tidal shear stress on the plate interface, leading them to suggest that tidal stresses could trigger or intensify large, high-amplitude RTRs that propagate in reverse into previously ruptured and weakened zones on the fault. *Beeler et al.* [2013] used observations of LFE sensitivity to tidal stressing on the San Andreas fault to constrain fault rheology. They assumed LFEs are generated on small patches that fail at a threshold stress on an otherwise creeping fault plane. These seismic patches are loaded tectonically, directly by the tides and also by time-dependent creep of the surrounding fault. The authors' analysis dismissed dislocation creep and dislocation glide as mechanisms for fault creep where LFEs occur, although rate-dependent friction is permitted if effective normal stresses are low, implying near-lithostatic pore pressures. Observations of high V_P/V_S ratios in the LFE source region in Cascadia [*Audet et al.*, 2009] and southwest Japan [*Shelly et al.*, 2007b] supply supporting evidence for near-lithostatic pore pressures in the subduction zone setting.

The aforementioned studies clearly establish that slow slip and tremor are modulated by tidal forcing. In this paper, we analyze the sensitivity of LFEs to tidal forces using three LFE detection catalogs for northern Cascadia, beneath southern Vancouver Island, and Washington state. LFE catalogs determined using network correlation hold advantages over tremor in that the LFE source locations and their temporal recurrence are more precisely defined, enabling detailed studies of spatiotemporal variability on discrete fault patches [*Shelly et al.*, 2007a; *Thomas et al.*, 2012]. Following the methodology proposed by *Thomas et al.* [2012], we quantify the correlation of our LFE families with tidal stresses, analyze the phase of LFE failure time relative to tidal load, compute the sensitivity to tidal shear stress as a function of time into an ETS event, and compare the sensitivity of LFEs at the leading edge of slip with that of LFEs contributing to "secondary events." We define "secondary events" as a generic term for slip fronts that occur after the main front has passed and refer to secondary events with similar characteristics to those identified in *Houston et al.* [2011] as RTRs. We compare results with previous work in Cascadia, Parkfield, and Shikoku and discuss the implications of these observations for plate boundary properties.

2. Data

We employ three distinct LFE detection catalogs in northern Cascadia. The first LFE catalog, assembled by *Bostock et al.* [2012] for southern Vancouver Island (SVI), was culled to 93 geographically independent LFE families with a total of 148,847 detections from ETS episodes between 2003 and 2013. The two other LFE catalogs were assembled by *Royer and Bostock* [2013] for Washington state. The northern Washington (NW) catalog was regrouped into 100 geographically independent LFE families and includes a total of 60,527 detections from ETS episodes between 2007 and 2011. LFE locations for this catalog span the eastern flanks of the Olympic Peninsula to the western reaches of Puget Sound. The southern Washington (SW) catalog, regrouped into 49 geographically independent LFE families, includes a total of 22,868 detections from ETS episodes during the period 2007–2008, from a region to the southwest of Puget Sound. Figure 1 shows LFE family locations for the three different catalogs. LFE detection methodology, location procedure, depth profiles, and focal mechanisms for the three catalogs are presented in *Bostock et al.* [2012] and *Royer and Bostock* [2013].

3. Methodology

3.1. Tidal Model

Tidal stress calculations require both global and local models. The global model we use is TPXO7.2 (2010): Oregon State University solution, Version 7.2. [*Egbert et al.*, 1994]. The local model is a recent version of Some Programs for Ocean-Tide Loading (SPOTL) for the west coast of North America [*Agnew*, 2012]. This version of SPOTL calculates horizontal and shear strains from the solid Earth and load tides at the Earth's surface. To compute strain at depth on a dipping fault requires two modifications. First, we use the Boussinesq solution for a point load on a half space to compute depth-dependent Green's functions for the load tide calculations. These Green's functions are calculated using a rigidity of $\mu = 30$ GPa and Poisson's ratio, $\nu = 0.25$ [*Farrell*, 1972]. Second, we assume that the strains from the body tides do not vary substantially over the depth range of interest and are approximately equal to those at the surface. Assuming that normal stresses

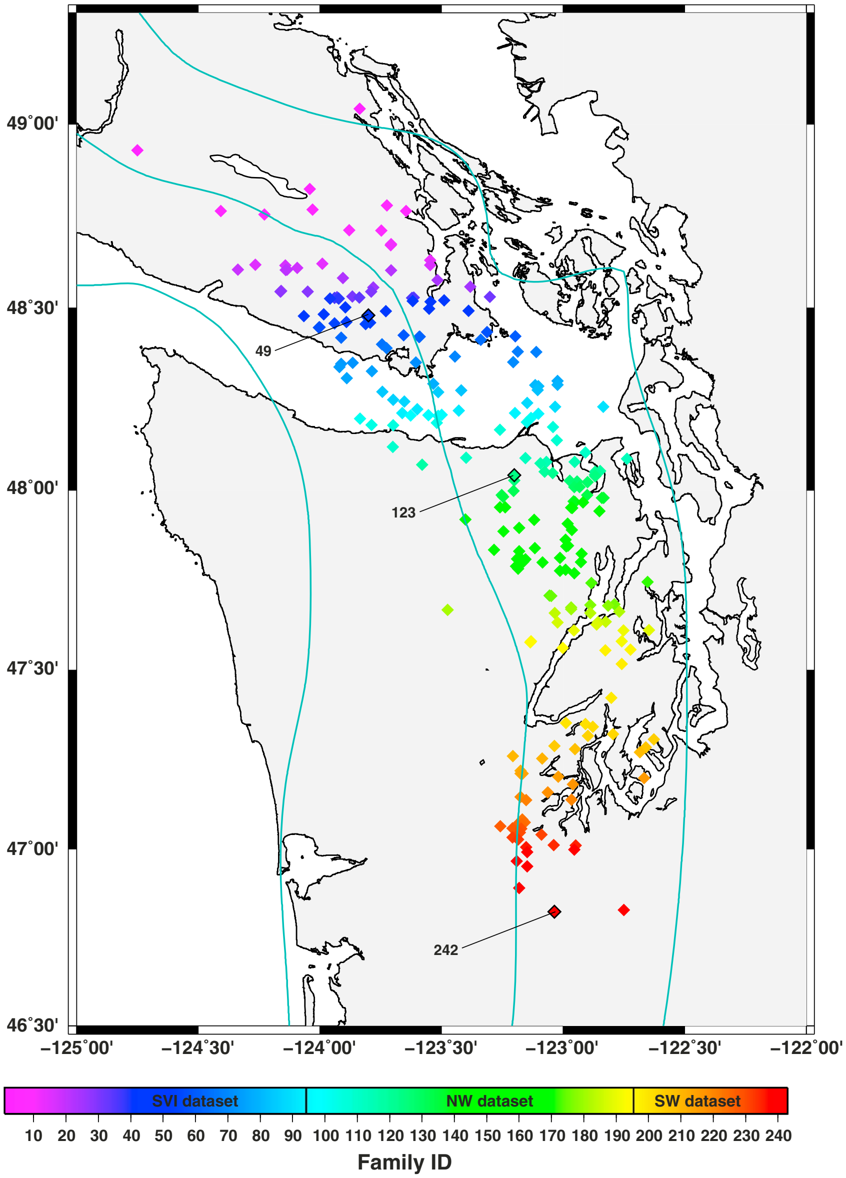

Figure 1. Map of LFE family locations in southern Vancouver Island (SVI detection catalog) and Washington State (NW and SW detection catalogs) assembled by *Bostock et al.* [2012] and *Royer and Bostock* [2013], respectively. Cyan lines indicate the 20, 30, and 40 km depth contours to the top of the subducting Juan de Fuca plate modeled by *Audet et al.* [2010]. Color bar legend indicates LFE family IDs ordered by latitude, from north to south, and the subdivision of the three detection catalogs is shown by black vertical lines. The three numbered families are used in the plots of Figure 2.

are zero at the Earth's surface, the vertical strain e_{rr} can be expressed in terms of the two horizontal strains $e_{\theta\theta}$ and $e_{\lambda\lambda}$ as follows [*Melchior*, 1978]:

$$e_{rr} = \frac{-\nu}{1-\nu}[e_{\theta\theta} + e_{\lambda\lambda}]. \tag{1}$$

We compute tidally induced fault normal and updip shear stresses, FNS and UDSS, and their time derivatives dFNS and dUDSS, using stress tensor time series and estimates of dip and dip azimuth of the subducting Juan de Fuca plate based on a smoothed version of the model of *Audet et al.* [2010] (note that depths are determined directly from LFE hypocenters, not the slab model). Comparisons with stress values determined for the slab geometry of *McCrory et al.* [2012] for a selection of LFE templates along the margin (#s 7,55,123,242) for the ETS episode in 2003 reveal some differences in amplitude, with a median absolute difference of 8% and a maximum amplitude change of a factor of 2. In general, changes in phase are small

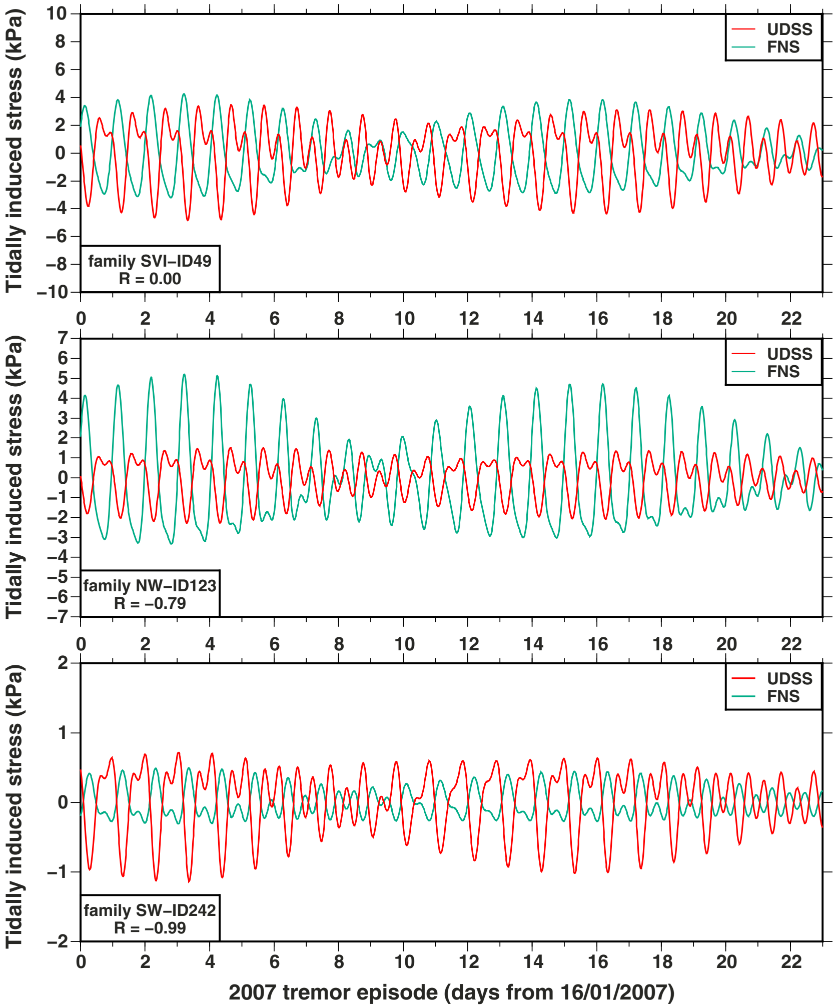

Figure 2. The 2007 tremor episode time series of tidally induced UDSS (red) and FNS (green) for (top) LFE family 49 from the SVI detection catalog, (middle) LFE family 123 from the NW detection catalog, and (bottom) LFE family 242 from the SW detection catalog. The correlation coefficient *R* between FNS and UDSS for the given family is indicated in each panel.

and vary by at most 1 h. These differences result primarily from differences in strike and dip between the two interface models. Positive FNS indicates extension and positive UDSS refers to thrust-promoting shear stress in the updip direction. These four tidal time series are computed at sample intervals of 15 min for each tremor episode in the period 2003–2013. Figure 2 shows an example of tidal time series FNS and UDSS for LFE families 49 (SVI), 123 (NW), and 242 (SW) (see Figure 1 for locations). Figure 3 maps the time-averaged envelope amplitude of stress of each LFE family for the four tidal components, computed as the magnitude of the analytic tidal signal over the corresponding detection period. Envelope amplitudes for UDSS and dUDSS increase from south to north, ranging from 481 Pa to 2276 Pa for UDSS, and between 2.6 Pa/min and 17 Pa/min for dUDSS. In contrast, envelope amplitudes for FNS and dFNS are larger beneath the Strait of Juan de Fuca, where the ocean load tides have a stronger influence. The amplitudes vary between 95 Pa and 5293 Pa for FNS, and between 0.42 Pa/min and 26 Pa/min for dFNS.

For 50% of the LFE locations, FNS and UDSS time series are anticorrelated with a coefficient correlation lower than −0.5. We may explain this negative correlation between FNS and UDSS by considering the relative contributions from different tidal components. The ocean load tides exert a stronger influence on the stresses in the tremor zone of northern Cascadia than the body tides by a factor that ranges from 2 to 10. This load tide influence can be divided into three components: the long wavelength load on the oceanic plate seaward of the trench, loading on the continental slope and shelf, and the load contribution from the inland seas, namely, Georgia Strait and Puget Sound. The first contribution is the least important on account of its

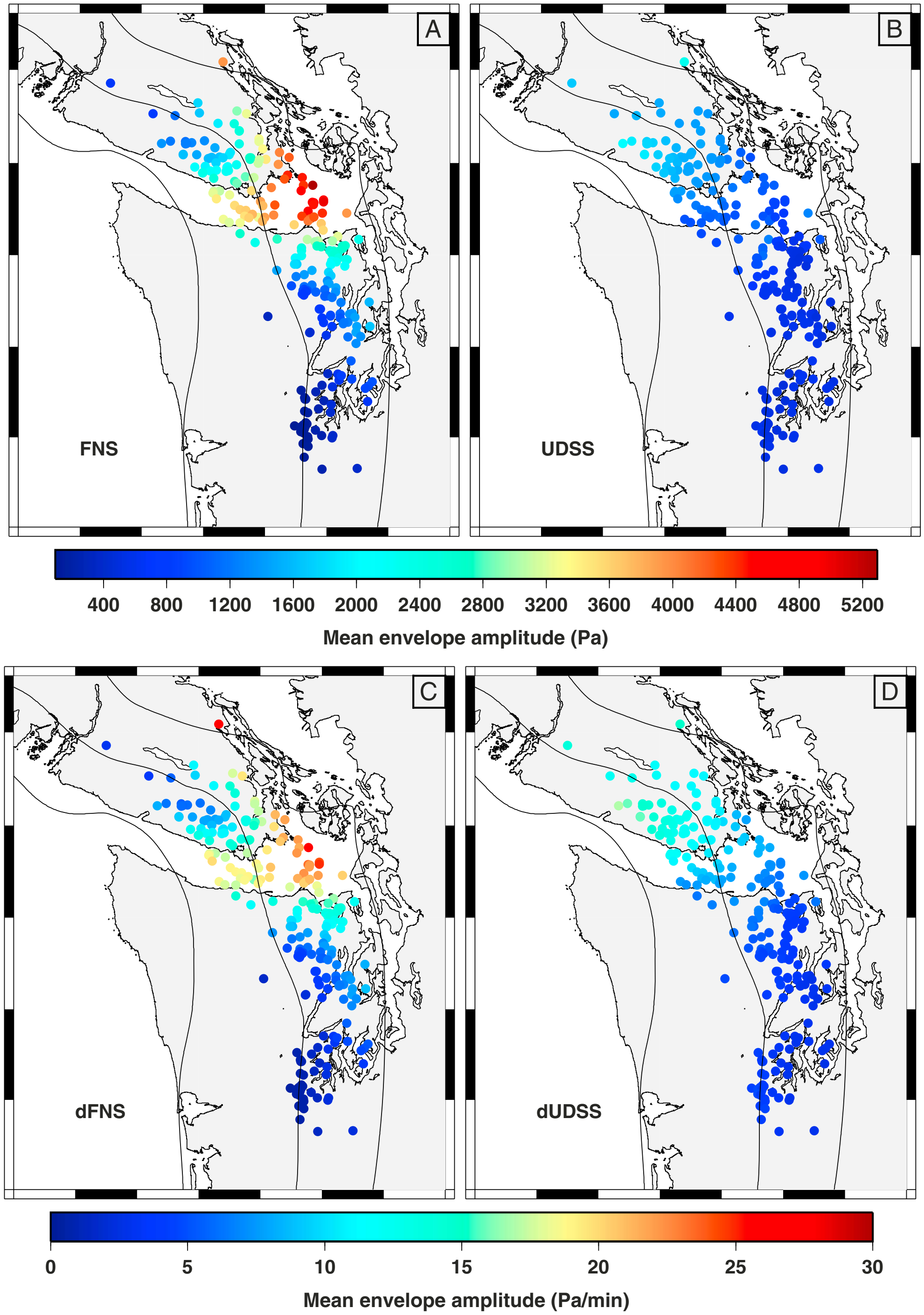

Figure 3. Map of tidal stress amplitudes. Mean tidal envelope amplitudes over detection time intervals are plotted color coded at locations of LFE families: (a) FNS, (b) UDSS, (c) dFNS, and (d) dUDSS time series.

distance (the trench lies some 100 km southwest of the coast). As explained by *Lambert et al.* [2009], the two latter contributions are nearly opposite in phase and so contribute constructively to UDSS and destructively to FNS on that portion of the plate boundary where ETS occurs (roughly midway between the two water bodies). The offshore coastal load produces oppositely signed UDSS and FNS on the plate boundary and outweighs the contribution from the inland seas, with the result that FNS and UDSS are anticorrelated. In contrast, LFE locations beneath the Strait of Juan de Fuca (roughly 25% of the total) display the largest

FNS envelope due to the additional load contribution from the Strait of Juan de Fuca resulting in weaker correlation between FNS and UDSS.

3.2. LFE Correlation With Tidal Stress

For each LFE family location, we compute the tidally induced stresses and their derivatives at times corresponding to detections and compute the expected number of detections based on the amount of time spent in a particular loading condition (first relative to the sign of tidally induced stresses and stress rates, and later to the stress-magnitude range), assuming that LFE detections occur randomly in a given tremor episode. We quantify the degree of correlation of LFE occurrence with tidal stress by computing the excess value:

$$N_{\mathrm{ex}} = \frac{\#\,\text{observed detections} - \#\,\text{expected detections}}{\#\,\text{expected detections}}. \tag{2}$$

Positive N_{ex} values indicate a surplus of detections in the loading condition considered, and negative N_{ex} values indicate a deficit of detections. We include 95% and 99% confidence intervals by generating 25,000 random catalogs of N detections each (the number N varies with the LFE family considered, between 386 and 3575 for SVI, between 141 and 1942 for NW, and between 204 and 895 for SW) to compute a distribution of N_{ex} values. N_{ex} values that fall outside the 99% confidence interval are less than 1% likely to occur randomly assuming that tides and LFEs are uncorrelated. Figure 4 shows a map of LFE family locations, color coded by N_{ex} values corresponding to the four tidal components.

We consider how specific stress levels influence LFE occurrence by computing LFE rates as a function of the magnitude of the applied stress components. We determine the observed number of LFE detections for a particular family that falls within a given stress range (40 bins over the total stress range, set independently for each of the FNS, UDSS, dFNS, and dUDSS time series). The expected number of detections in each bin is then computed based on the null hypothesis that LFE origin times and tides are uncorrelated. The ratio for each bin for a given stress component and for all families is given by

$$\frac{\#\,\text{observed detections}}{\#\,\text{expected detections}} = N_{\mathrm{ex}} + 1. \tag{3}$$

Ratios greater than 1 translate to a surplus of detections, and ratios lower than 1 indicate a deficit of detections compared to a random detection distribution. Results are plotted in Figure 5.

We assign an effective phase angle to each LFE detection of a particular family using a method similar to that of *Tanaka et al.* [2002]. For each of the two pairs of components UDSS, dUDSS and FNS, dFNS, the maximum and the minimum tidal stresses are assigned to 0° and ±180°, respectively. However, in an extension of this approach, the maximum and minimum tidal stress rates correspond to 90° and −90°, respectively, increasing the accuracy of our assigned effective phases. The effective phase is assigned by interpolating the time of the event between times with assigned phases. We assemble the observed numbers of detections that fall within a phase angle range (here we consider 36 bins of 10°), and the expected numbers of detections in each bin are computed based on the null hypothesis that LFEs and tides are randomly correlated. We compute again the ratio $N_{\mathrm{ex}}+1$ for each bin of a given component pair (FNS,dFNS and UDSS,dUDSS) and for all families. Rose histograms of tidal phases for the three different LFE detection catalogs are plotted in Figure 6. A schematic phase plot with labeling is provided to aid in understanding the rose histograms. Bins that contain the expected number of detections have a radius of 1 (100% of the expected values assuming a random distribution shown by red contour). Confidence intervals corresponding to the 95% and 99% levels are also provided on each polar histogram (blue contours).

3.3. Time-Dependent Tidal Sensitivity

Lambert et al. [2009] (Figure 3 in their paper) commented that the response of Vancouver Island tremor detections to tidal stress varies through a tremor episode increasing from near zero to a finite level before falling back to zero. *Thomas et al.* [2012] observed that deep LFE families on the San Andreas fault that occur continuously generally had greater tidal sensitivity than shallower, episodic families. They interpreted the episodic families as having larger background slip rates than the continuous ones and suggested that the magnitude of tidal correlation decreases during strongly accelerated fault slip. H. Houston [*Houston*, 2013, also Response of tremor and slow slip to tidal stress: Constraints on fault friction and weakening, submitted to *Nature Geoscience*, 2014] has also observed that tremors in Washington and SVI [*Wech and Creager*, 2008] are more sensitive to tidal stressing after the main slip front has passed. Here we investigate

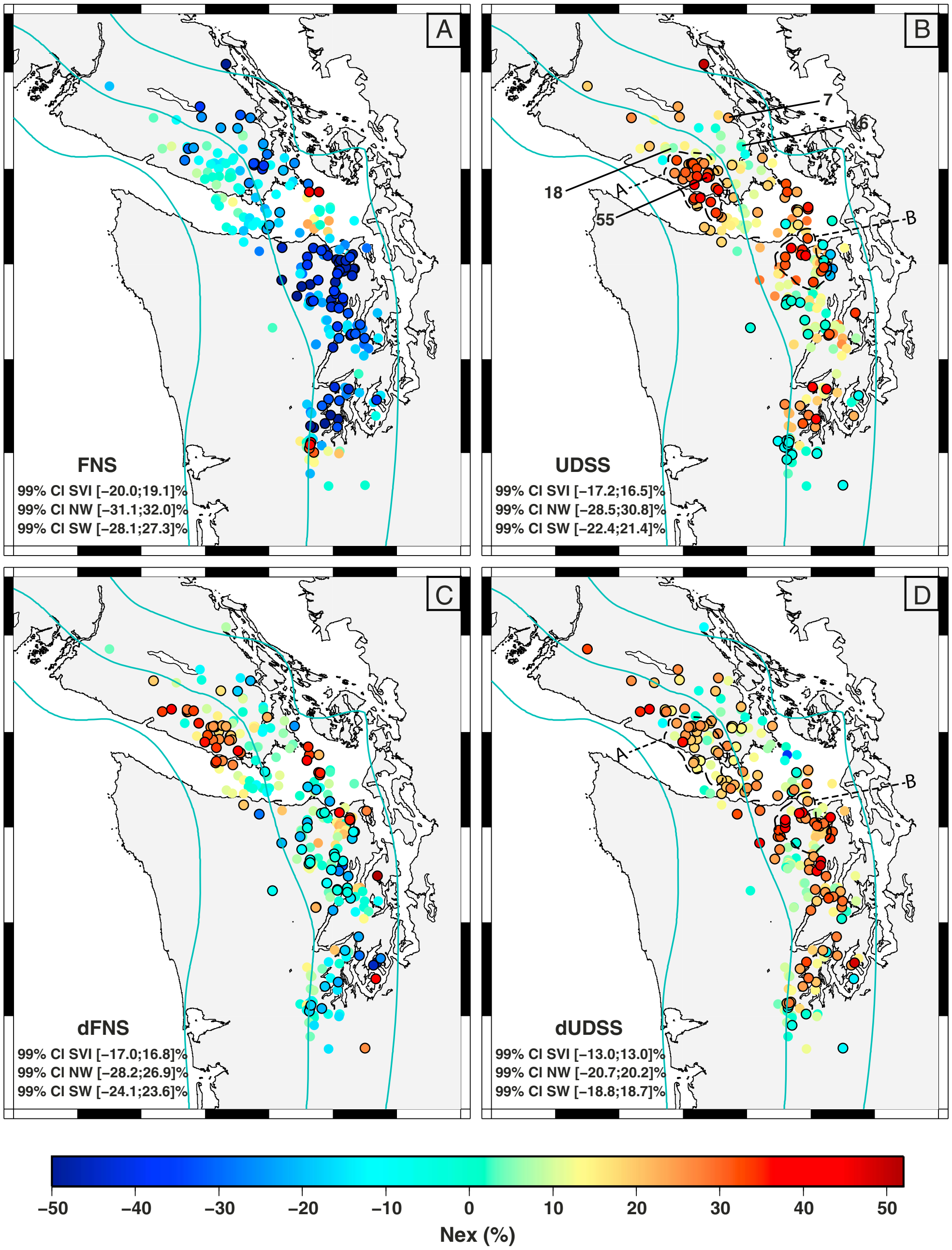

Figure 4. Map of N_{ex} values relative to the positive sign of tidally induced stresses and stress rates. LFEs are color coded by N_{ex} values corresponding to the (a) tidal FNS, (b) UDSS, (c) dFNS, and (d) dUDSS components. The 99% confidence intervals (CI) calculated for the family with the fewest detections are given in the bottom left of each panel for each detection catalog, and significant families are indicated with black rims. The four numbered families in Figure 4b are used in the recurrence analysis (section 5.3).

this dependence using our LFE catalogs. Most LFE families, independent of the ETS episode considered, display a steep increase in cumulative detections over the first day or two that levels off gradually thereafter. *Rubin and Armbruster* [2013] report similar behavior in their study of LFEs in Vancouver Island and note that the LFE detection rate starts high and gradually decays over the course of a few days, becoming increasingly intermittent. We define by visual inspection the beginning of LFE activity for a particular LFE family as the onset of the steep slope of their corresponding cumulative distributions. The percent excess value N_{ex} for the positive UDSS loading condition is computed for each of the 8 days following the beginning of activity. Figure 7 displays UDSS N_{ex} histograms (green bars) assembled for all families and all years (Figure 7, left

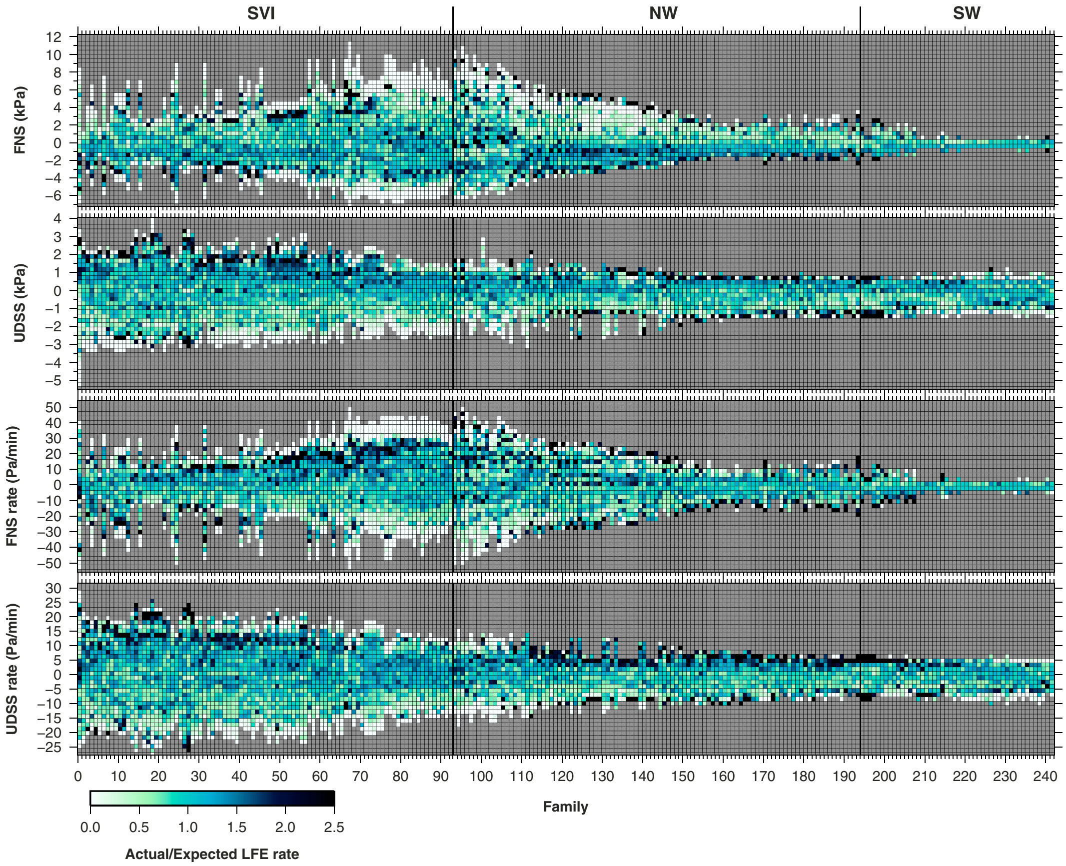

Figure 5. (from top to bottom) LFE rate plots as a function of the magnitude of the (first panel) FNS, (second panel) UDSS, (third panel) dFNS, and (fourth panel) dUDSS components. Each column corresponds to an individual LFE family (ordered from north to south, all detection catalogs combined—subdivision shown by black vertical lines), and each row corresponds to a stress interval. The ratio of observed/expected number of LFE detections within a stress range is color coded with dark colors (surplus of LFE detections, ratio greater than 1) and light colors (deficit of LFE detections, ratio lower than 1) as shown on the color bar legend.

column), for subgroups of LFEs with high N_{ex} (regions A and B, $N_{ex} > 30\%$—Figure 7, middle column—see section 4) and for subgroups of LFEs with low N_{ex} values ($N_{ex} < 10\%$, Figure 7, right column) for the SVI and NW regional catalogs. Confidence intervals at the 95% and 99% levels are indicated by the blue and red bars, respectively, and are determined by generating 25,000 random catalogs of M detections each (the number M corresponds to the number of detections contributing to each 1 day interval) to compute a distribution of N_{ex} values (as in (2)) for each day. Superimposed on the histograms are the percent cumulative distribution of LFE detections (blue curve) with the number of detections contributing to each 1 day interval indicated at the bottom of each panel. We investigate time-dependent phase shifts by computing $N_{ex} + 1$ for the positive UDSS loading condition for each of the 8 days following the beginning of activity. Rose histograms of UDSS tidal phase for SVI are plotted in Figure 8. Corresponding phase plots for NW and SW can be found in Figures S1 and S2 in the supporting information.

3.4. Tidal Sensitivity and Stress Drop of RTRs Versus the Main Front

Thomas et al. [2013] noted that large, high-amplitude RTRs [*Houston et al.*, 2011] in northern Washington occur almost exclusively during times of positive UDSS. We recall that RTRs (Rapid Tremor Reversals) are secondary events occasionally propagating rapidly in the opposite direction from the advancing tremor and slip front. We use time-distance plots of our SVI LFE catalog to identify RTRs on southern Vancouver Island and examine their sensitivity to UDSS. For each tremor episode, we project LFE family locations onto an along-strike profile and plot distance-along-strike versus time. We identify subjectively RTRs as linear streaks of LFE detections moving at high apparent velocities in the opposite direction to the main slip front. Figure 9 shows the location of the along-strike profile (Figure 9a) as well as time-distance plots for the 2003 and 2012

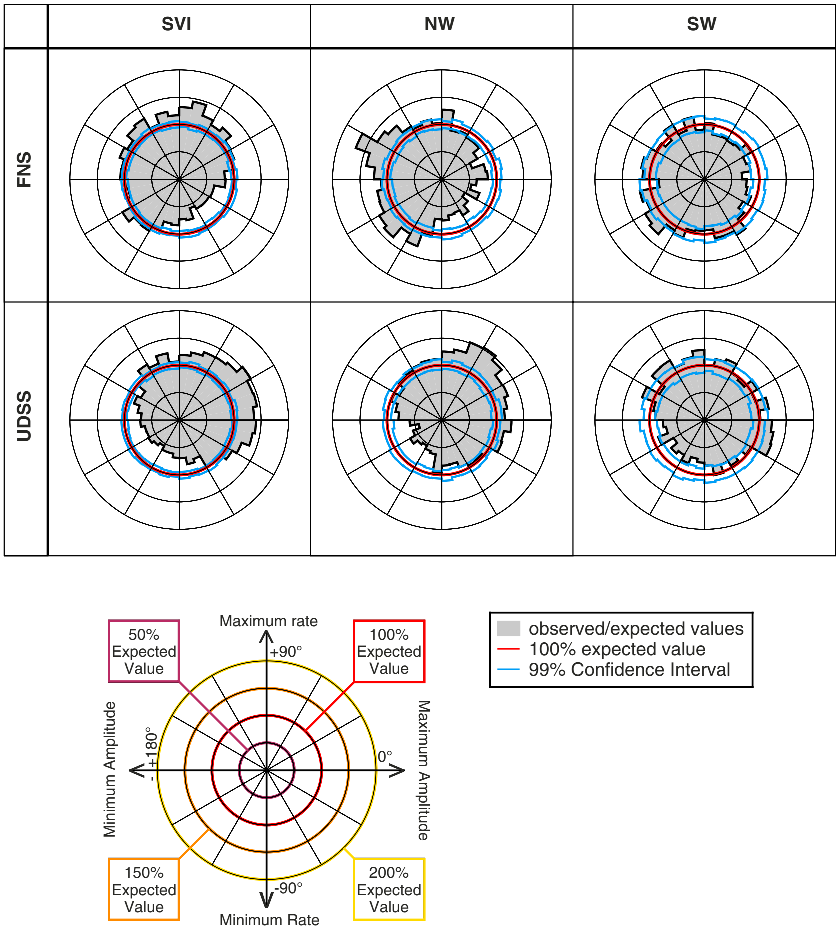

Figure 6. (bottom) Schematic phase plot labeling the 50%, 100%, 150%, and 200% expected value contours. (top) Tidal phase histograms. (top row) FNS and (bottom row) UDSS phase plots for a stack of all detections from (left) SVI, (middle) NW, and (right) SW detection catalogs. Gray shaded areas indicate ratio of observed over expected number of detections in each 10° phase bin. Blue lines are the lower and upper limits of the 99% confidence intervals for each bin. Red lines are the 100% expected value contours.

tremor episodes (Figure 9b). Note that in 2012, the main slip front propagated from NW to SE, opposite its usual direction. For each RTR, we determine the duration, the along-strike distance of propagation, and the along-strike velocity. Results for all tremor episodes for which RTRs were confidently identified are reported in Tables 1 and 2. For each LFE family, we determine the percentage of detections that take place as part of RTRs and we compute N_{ex} values corresponding to positive UDSS for both RTR detections and non-RTR detections (the latter defined as detections that are not part of RTRs). A summary of results is presented in Table S3 of the supporting information.

Following *Rubin and Armbruster* [2013], we estimate an order of magnitude contribution from the RTR events to the total stress drop $\Delta\tau$ for a given LFE as follows:

$$\Delta\tau = \frac{\#\text{ detections in an RTR}}{\#\text{ total detections}} \frac{D\mu}{L_s\pi}, \tag{4}$$

where D is the total slip accumulated at an LFE location during a tremor episode, that is, $D \approx 2$ cm according to geodetic estimates [*Szeliga et al.*, 2008; *Wech et al.*, 2009; *Schmidt and Gao*, 2010], $\mu = 18$ GPa is the shear modulus (assuming $V_p = 6000$ km/s, $V_p/V_s = 2.45$ and $\rho = 3000$ kg/m^3), and L_s is the width of the main slip front. We can estimate the latter quantity by considering the time interval during which a given LFE is active (within an individual RTR or as part of the main front) and multiplying by the along-strike velocity (assuming propagation is dominantly along strike). Using the information in Tables 1 and 2, and Figure 9 we find that $L_s \approx 5$ km/d $\times$ 2 days ≈ 5 km/h $\times$ 2 h ≈ 10 km (2 h corresponding to the characteristic duration of an RTR at

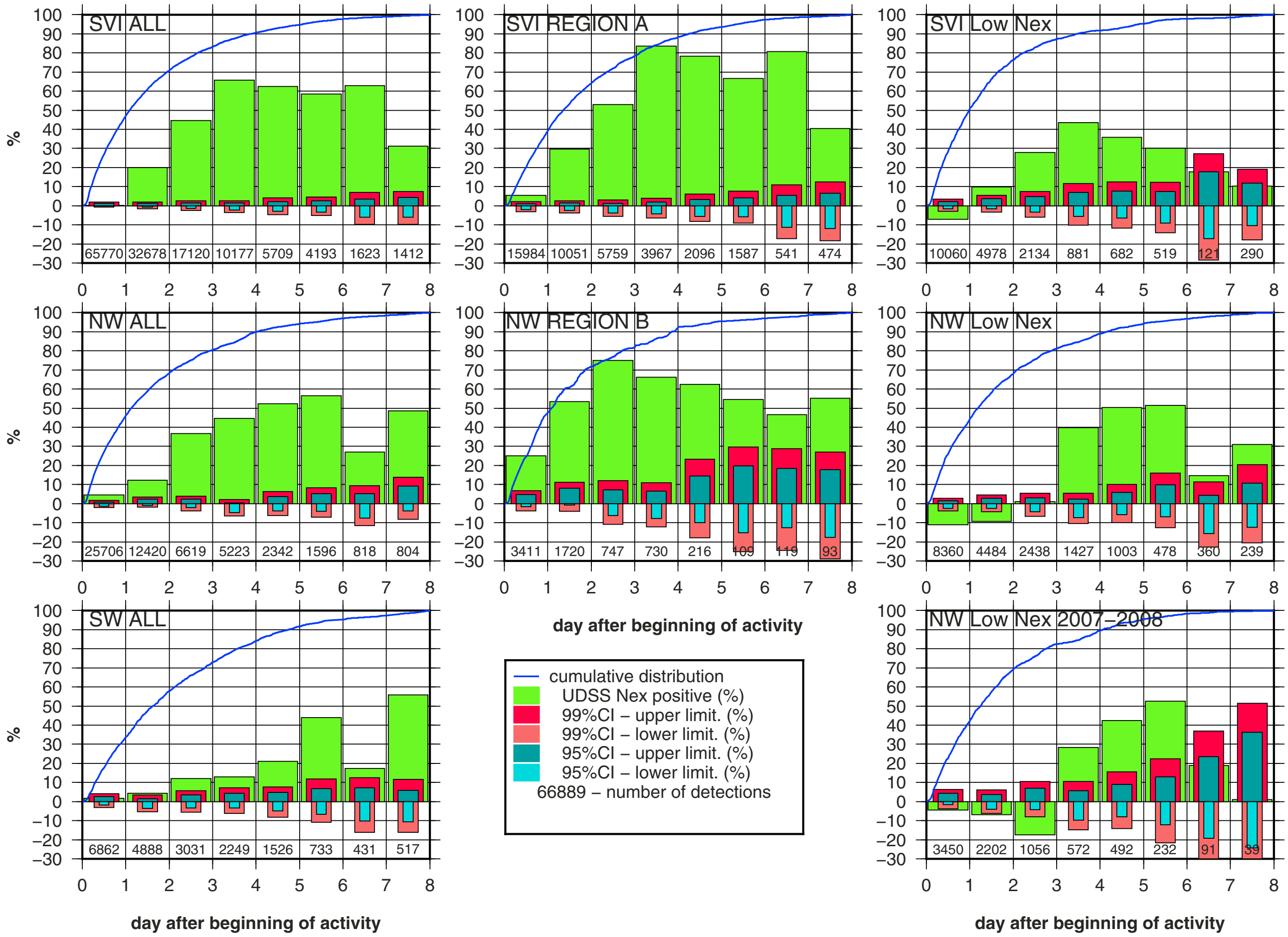

Figure 7. N_{ex} UDSS histograms for positive tidal forcing for the (top row) three detection catalogs SVI, (middle row and bottom right) NW and (bottom left) SW. N_{ex} UDSS is computed every day up to 8 days after the beginning of activity. The percent cumulative detection distributions for each catalog is provided (blue curve), and the associated number of detections in each 1 day interval is given at the bottom of each panel. Lower and upper limits of 95% and 99% confidence intervals are given, distinguished by blue and red color bars, respectively.

a given LFE family location). That is, order of magnitude estimates of the widths L_s of the actively slipping regions appear to be of the order of 10 km for the main front and RTRs.

3.5. Diurnal Variation of LFE Occurrence

Motivated by the observations of *Rubinstein et al.* [2008] and *Lambert et al.* [2009], we investigate LFE correlation with a previously described diurnal signal. *Rubinstein et al.* [2008] identified a strong peak in tremor spectra between 24 and 25 h period and noted that the peaks of the envelope corresponding to the ~ 24 h period component of tremor do not correlate with daylight hours, when cultural noise is at its maximum. In contrast, the Vancouver Island study of *Lambert et al.* [2009] presented evidence for a significant, nontidal, daily variation in tremor activity, with higher sensitivity at midnight than at noon when noise levels are generally higher. To shed further light on the nature of this signal, we determine N_{ex} values for LFE detections falling within a given hour of the day, with results plotted in Figure 10.

4. Results

4.1. LFE Correlation With Tidal Stress

A concentration of LFE families in southern Vancouver Island in an updip region of high slab curvature centered near 48.43°N, 123.83°W, hereafter “region A,” shows strongest correlation to tidal forcing during periods of positive and increasing UDSS (Figures 4b and 4d). In Washington state, the strongest correlation to tidal forcing during periods of positive and increasing UDSS (Figures 4b and 4d) occurs for a more diffuse distribution of LFE families near the town of Sequim (hereafter “region B”). These two regions display a large surplus of detections with positive UDSS ($N_{ex} > 30\%$) and positive dUDSS ($N_{ex} > 3\%$ up to 44%) at a

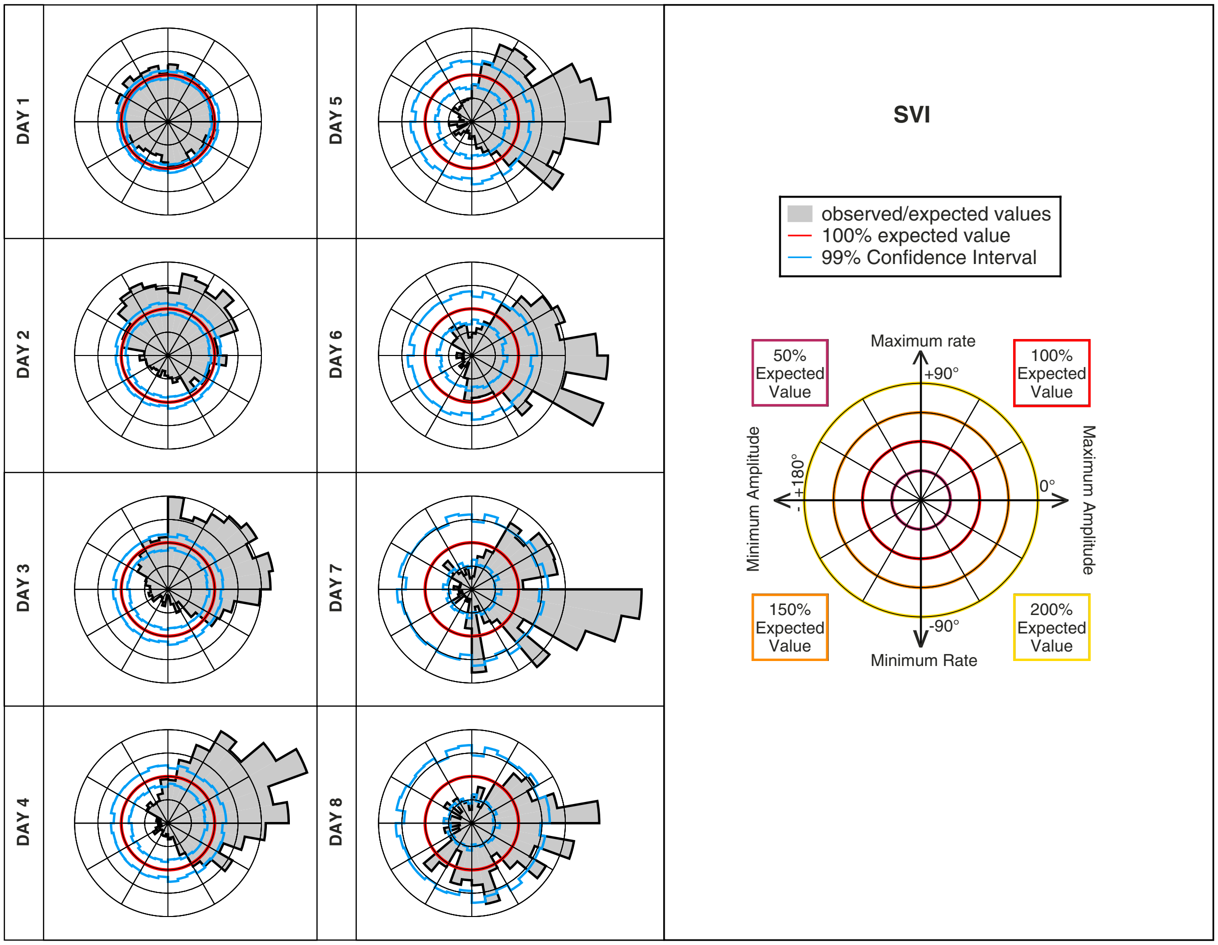

Figure 8. (right) Schematic phase plot labeling the 50%, 100%, 150%, and 200% expected value contours. (left and middle) Tidal phase histograms. UDSS phase plots for a stack of all detections from SVI detection catalog every day up to 8 days after the beginning of activity. Gray-shaded areas indicate ratio of observed over expected number of detections in each 10° phase bin. Blue lines are the lower and upper limits of the 99% confidence intervals for each bin. Red lines are the 100% expected value contours.

significance level of 99% or greater. Away from these two regions, the distribution of N_{ex} values is generally more sporadic and disorganized. There appears to be little correlation between the mean tidal envelope amplitude and N_{ex} values for any of the four tidal components as shown in Figures 3 and 4, and Figure S4 in the supporting information despite the fact that tidal amplitudes vary by over a factor of 10 across the entire region. We note that the more equivocal signature of tidal sensitivity in the SW LFE catalog for most measures is most likely due to the reduced recording period for this array of stations, that is, two episodes versus 10 episodes for SVI.

A majority of LFE families display significant negative FNS N_{ex}. We performed a hypothesis test for spurious correlations (Figure S5—for methodology, see *Thomas et al.* [2012]). This analysis reveals that the correlation with FNS for many LFE families, particularly those families beneath SVI and the northeast Olympic Peninsula, cannot be explained by another stressing function.

Further details concerning the temporal dependence of LFEs within the stress cycle are revealed in Figure 5 which displays N_{ex} binned in constant intervals of stress and stressing rate. For LFE families in “region A” (LFE numbers 29, 33, 37–39, 44, 48–53, 55, 56, 63, 66, 72, 73, 75, and 84), the highest sensitivity to UDSS occurs close to the positive maximum of UDSS ($N_{ex} + 1 > 2$) between 1.5 and 2.0 kPa (Figure 5, middle top—UDSS), when UDSS is increasing ($N_{ex} + 1 > 1.5$) between 10 and 15 Pa/min (Figure 5, bottom—dUDSS). For LFE families in “region B” (LFE numbers 108, 112, 114, 119, 121, 123, 131, 133, 139, 146, and 147), the highest sensitivity to UDSS occurs close to the positive maximum of UDSS ($N_{ex} + 1 > 1.5$) between 1.0 and 1.5 kPa,

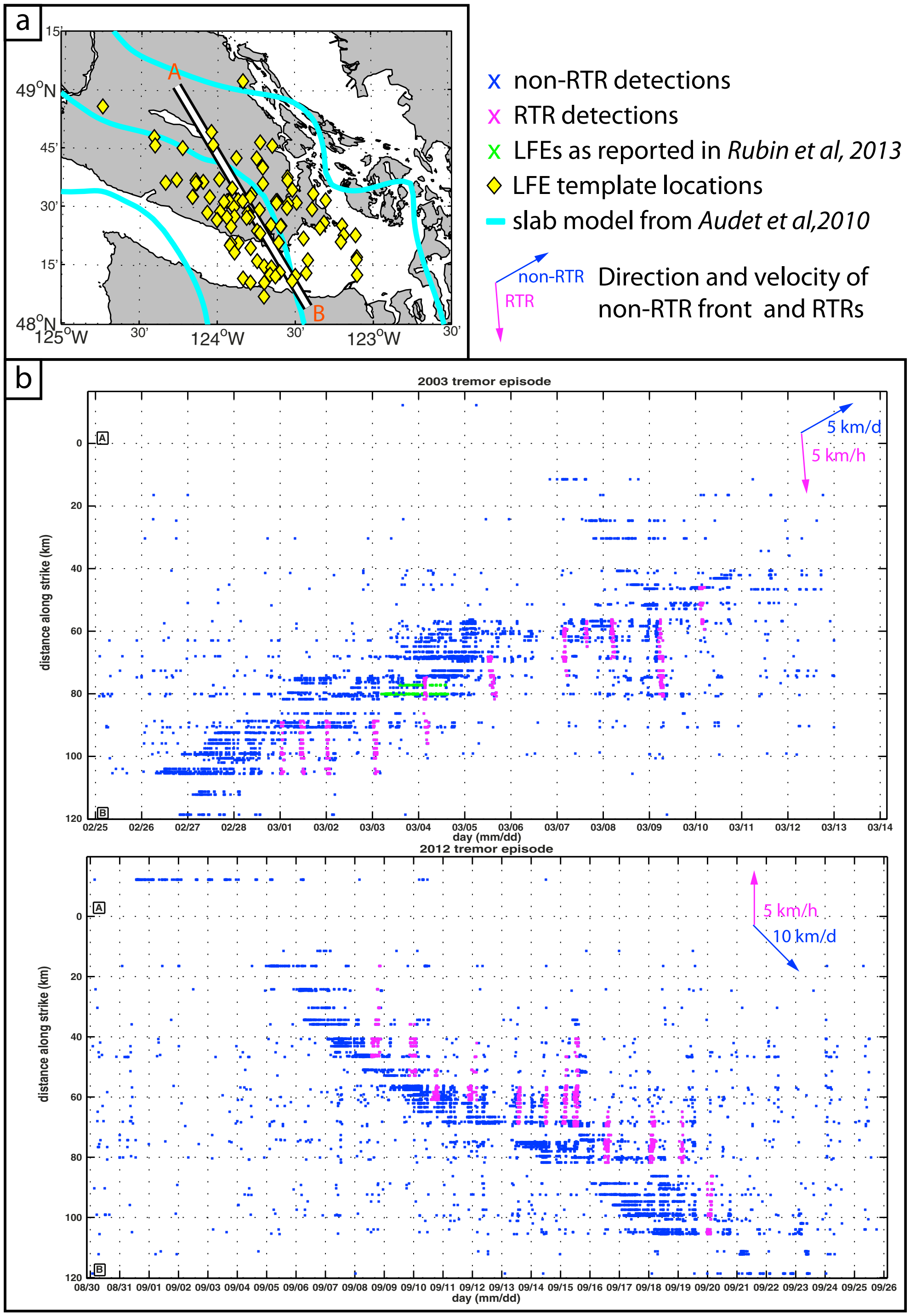

Figure 9. (a) Location of the along-strike profile used for the time-distance plot in Figure 9b and SVI LFE locations (yellow diamonds). Cyan lines indicate the 20, 30, and 40 km depth contours to the top of the subducting Juan de Fuca plate modeled by *Audet et al.* [2010]. (b) Time-distance plots for the 2003 and 2012 tremor episodes. Blue and magenta detections represent detections from non-RTR front and RTRs, respectively. Green detections represent LFEs that participated in the small-scale secondary fronts of 3 March 2003 as reported by *Rubin and Armbruster* [2013]. Direction and along-strike velocity of non-RTR front and RTRs are provided in each plot.

Table 1. RTRs Documentation for 2003–2005 and 2008

# RTR	Start Time[a]	End Time[a]	Duration (hh:mm)	Distance Along Strike (km)	Distance Along Dip (km)	Velocity Along Strike (km/h)
2003 - 1	1/3 00:23	1/3 02:10	1:47	16.2	7.9	9.1
2	1/3 10:25	1/3 12:53	2:28	16.7	9.5	6.8
3	1/3 23:36	2/3 01:50	2:14	16.7	9.5	7.5
4	2/3 23:56	3/3 03:17	3:31	16.7	9.5	5.0
5	4/3 02:43	4/3 05:24	2:41	20.8	10.2	7.8
6	5/3 11:59	5/3 15:20	3:21	13.4	11	4.0
7	7/3 02:36	7/3 05:03	2:54	14.9	10	5.1
8	7/3 14:26	7/3 15:59	1:33	8.1	4.7	5.2
9	8/3 03:49	8/3 07:17	2:28	12.4	11.8	5.0
10	9/3 04:36	9/3 07:44	3.08	24.5	12.7	7.8
11	10/3 10:49	10/3 04:56	3.07	13.4	6.1	4.3
2004 - 12	14/7 00:33	14/7 03:30	2:57	16.7	9.5	5.7
13	14/7 23:52	15/7 03:49	3:57	28.8	12.8	7.3
14	16/7 23:29	17/7 03:46	4:17	25.4	13.6	5.9
15	18/7 10:58	18/7 15:14	4:16	21.7	7.2	5.1
16	19/7 00:06	19/7 03:03	2:57	13.3	12.7	4.5
17	21/7 03:40	21/7 06:18	2:38	8.1	5.1	3.1
18	21/7 15:29	21/7 19:06	3:37	4.7	2.7	1.3
2005 - 19	11/9 13:24	11/9 18:39	5:15	19.1	9.5	3.6
20	12/9 03:51	12/9 00:47	4:56	14.2	7.4	2.9
21	12/9 20:56	13/9 00:33	3:37	13.1	6.1	3.6
22	13/9 21:54	14/9 03:09	5:15	19.8	7.1	3.8
23	14/9 22.12	15/9 01:29	3:17	25.4	10.0	7.6
24	15/9 06:44	15/9 11:00	4:16	10.4	6.9	2.4
25	15/9 22:50	16/9 02:46	3:54	13.4	6.9	3.4
26	16/9 23:28	17/9 03:04	3:36	12.5	6.8	3.5
27	18/9 00:45	18/9 06:59	6:14	43.1	7.1	6.9
28	19/9 11:14	19/9 17:09	5:55	22.3	8.7	3.8
2008 - 29	15/5 19:47	16/5 00:13	4:26	16.7	9.5	3.8
30	18/5 00:19	18/5 05:26	5:07	25.3	9.8	4.9
31	19/5 00:52	19/5 05:18	4:26	19.1	10.0	4.3
32	21/5 00:57	21/5 05:23	4:26	24.0	12.3	5.4
33	23/5 14:00	23/5 19:48	5:48	21.2	5.8	3.7
34	27/5 04:18	27/5 09:25	5:07	17.0	10.4	3.3

[a] Dates in Start Time and End Time columns are formatted as day/month.

when UDSS is increasing ($N_{ex} + 1 > 1.5$) between 5 and 10 Pa/min. The more northerly LFEs of the SW data set are sensitive to positive and increasing UDSS, but the general sensitivity is less obvious for the entire SW data set.

The overall sensitivity of all families to positive UDSS, dUDSS is also apparent in the stacked phase plots in Figure 6. For SVI and NW catalogs, the majority of LFEs fail during times of large, positive UDSS and large, positive UDSS rate, with at least one preferential failure time at radial values above 150% of the expected value and with an $N_{ex} + 1$ value exceeding the 99% confidence interval. This leads to a ~40° and ~60° phase advance (or considering the 12.4 h dominant tidal period, a ~1.3 and ~2 h advance) in the time of the peak radial value with respect to peak UDSS, for SVI and NW data sets, respectively. As for previous measures, the tidal sensitivity for the SW catalog is less clear. A majority of LFEs fail during times of large positive UDSS but negative dUDSS, above 100% of the expected value and with an $N_{ex} + 1$ value exceeding the 99% confidence interval.

Table 2. RTRs Documentation for 2010–2012

# RTR	Start Time[a]	End Time[a]	Duration (hh:mm)	Distance Along Strike (km)	Distance Along Dip (km)	Velocity Along Strike (km/h)
2010 - 35	22/8 21:15	23/8 00:47	2:52	16.7	9.5	5.8
36	24/8 00:39	24/8 03:47	3:08	16.7	9.5	5.3
37	24/8 23:06	25/8 02:46	2:40	16.7	9.5	6.3
38	25/8 10:51	25/8 14:15	3:24	16.7	9.5	4.9
39	26/8 22:52	27/8 02:32	3:40	23.3	12.3	6.3
40	27/8 22:53	28/8 01:46	2:53	11.4	11.3	4.0
41	28/8 15:04	28/8 18:12	3:08	12.5	6.8	4.0
42	29/8 13:31	29/8 16:08	2:37	7.1	4.7	2.7
43	31/8 02:35	31/8 06:30	3:55	17.0	8.1	4.3
44	02/9 03:24	02/8 06:48	3:24	22.7	4.7	6.7
2011 - 45	22/8 23:39	23/8 02:29	2:50	16.7	9.5	5.9
46	23/8 21:09	23/8 23:59	2:50	16.7	9.5	5.9
47	25/8 22:31	26/8 02:32	4:01	16.7	9.5	4.2
48	26/8 07:58	26/8 11:45	4:47	11.9	6.5	2.5
49	29/8 11:20	29/8 16:32	5:12	21.0	6.7	4.0
50	30/8 13:05	30/8 15:13	2:08	12.5	6.8	5.9
51	31/8 00:40	31/8 02:47	2:07	9.0	10.9	2.5
52	01/9 02:53	01/9 05:01	2:08	8.2	10.9	3.8
2012 - 53	8/9 13:17	8/9 21:02	7:45	29.5	18.2	3.8
54	9/9 20:19	10/9 02:15	5:56	17.0	10.0	2.9
55	10/9 13:40	10/9 20:58	7:18	10.0	7.6	1.4
56	11/9 19:20	12/9 03:33	8:13	18.9	9.3	2.3
57	13/9 12:25	13/9 16:31	4:06	12.0	10.8	2.9
58	14/9 10:19	14/9 13:58	3:39	12.0	16.3	3.3
59	15/9 01:23	15/9 05:29	4:06	22.2	12.6	5.4
60	15/9 10:31	15/9 14:37	4:06	19.0	11.6	4.6
61	16/9 11:37	16/9 17:06	5:29	16.9	10.0	3.1
62	18/9 00:35	18/9 06:04	5:29	16.9	10.0	3.1
63	19/9 00:47	19/9 04:53	4:06	16.9	10.0	4.1
64	19/9 22:41	20/9 04:37	5:56	19.2	9.5	3.2

[a] Dates in Start Time and End Time columns are formatted as day/month.

4.2. Time-Dependent Tidal Sensitivity

Figure 7 displays the sensitivity of LFE occurrence as measured by N_{ex} to positive UDSS forcing as a function of time. For SVI (Figure 7, top) and NW (Figure 7, middle) catalogs and all families and years considered (Figure 7, left), sensitivity rises steeply from near zero on the first day of strong activity to a maximum ∼4 days later for SVI and ∼6 days later for NW. Similar behavior is observed when catalogs are divided into subsets with high N_{ex} values (region A from SVI and region B from NW) and subsets with low N_{ex} values, with a shift in the maximum N_{ex} to 3 days or so later for region B. Although there is indication of a sustained increase in UDSS sensitivity 6 days after the initial onset of LFE activity for families in the SW catalog, this pattern cannot be confirmed at the same confidence levels as the two other catalogs.

In Figure 8, we present stacked phase plots of SVI LFEs with respect to UDSS as a function of time in days after the onset of strong activity. LFE occurrence shows little correlation to tidal phase on the first day of activity but, in subsequent days, transitions from a correlation with dUDSS to a correlation with UDSS. Similar behavior is evident for NW and, to a lesser extent, SW LFEs (see Figures S1 and S2 in the supporting information).

4.3. Tidal Sensitivity and Stress Drop of RTRs Versus the Main Front

For seven tremor episodes (2003–2005, 2008, and 2010–2012) in southern Vancouver Island, we identify by visual inspection a total of 64 RTRs (Tables 1 and 2 and Figure 9). RTRs that have N_{ex} values that greatly

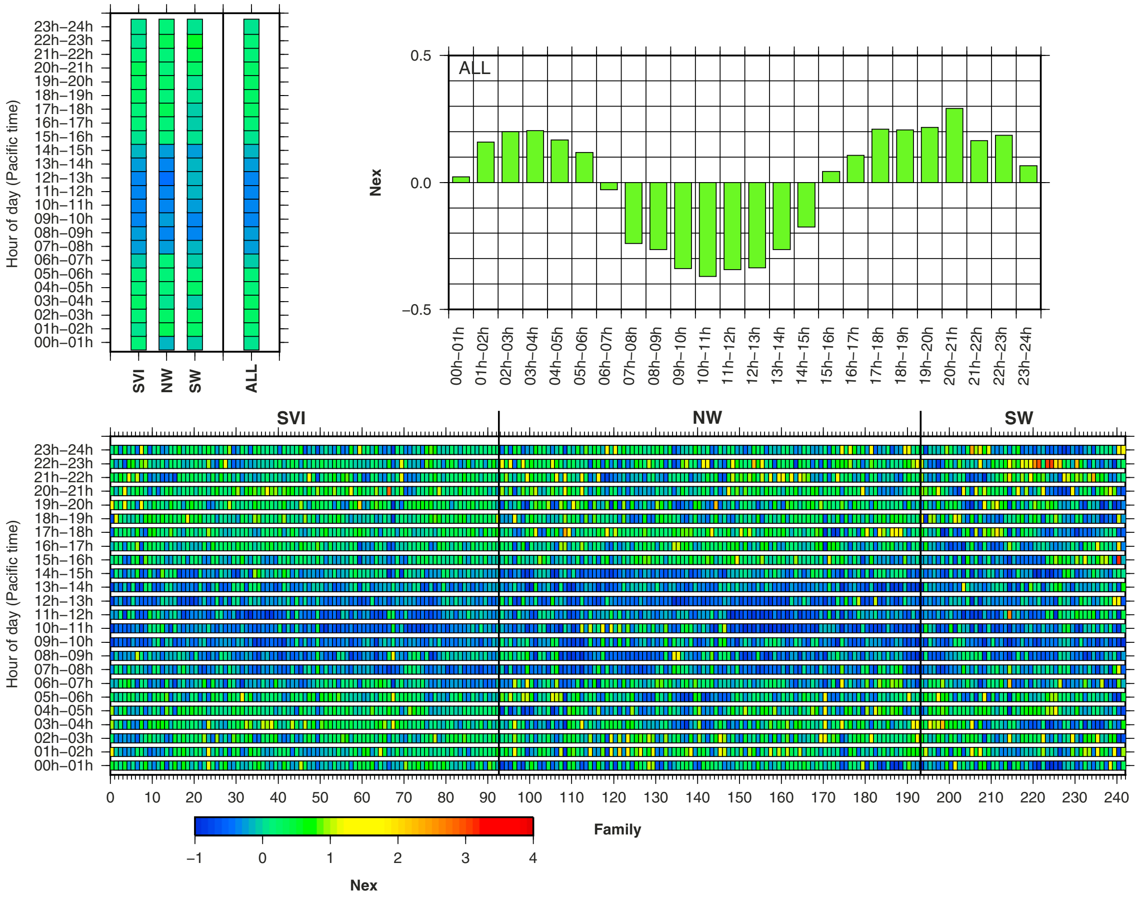

Figure 10. LFE rate plots as a function of hour of day (Pacific time). Each column corresponds to an individual LFE family (ordered from north to south, all detection catalogs combined—subdivision shown by black vertical lines), and each row corresponds to an hour interval. N_{ex} values in each hour range is color coded with colors as shown on the color bar legend. Blue colors represent a deficit of LFE detections ($N_{ex} < 0$), whereas green, warm colors represent a surplus of LFE detections ($N_{ex} > 0$).

exceed those of the main front, propagate along strike at an average speed of 5 km/h and have an average duration of 4 h. We note that, during RTRs, the non-RTR events that constitute the main front continue producing tremor. Our observations indicate that 6.8% of all detections per episode occur within individual RTRs (i.e., the ratio of detections required in (4)) as averaged over all LFE families and ETS episodes. Moreover, as many as one third of all detections for a given LFE family can occur within RTRs (see Table S3 in the supporting information), and a majority (72%) of RTRs occur exclusively during periods of positive UDSS. We further note that, in general, LFE families in “region A” possess a higher percentage of RTR events (>20%). However, some LFE families with lower sensitivity to UDSS (south of “region A” and few downdip families) also possess high percentage of RTR events. We compute the stress drop associated with LFEs that are participants in 64 RTRs for a total of 1312 “ruptures” (or LFE-RTR combinations). The mean stress drop is ∼0.8 kPa, an order of magnitude smaller than that associated with the main slip front (and secondary fronts analyzed by *Rubin and Armbruster* [2013]).

5. Discussion

We now proceed to examine the implications of our observations of the tidal modulation of LFEs in northern Cascadia for our general understanding of the slow slip process.

5.1. Spatial Distribution of Tidal Sensitivity

The population of LFEs beneath the northeast Olympic Peninsula and beneath SVI that correlate with compressional normal stress is enigmatic. Several authors have shown that tremor and LFEs are primarily sensitive to variations in tidally induced shear stresses and often do not respond to larger normal stress variations [*Thomas et al.*, 2009; *Hawthorne and Rubin*, 2010; *Thomas et al.*, 2012]. A few events in *Thomas et al.* [2012] did appear to have negative FNS correlation that those authors attributed to a releasing right bend along the San Andreas fault. The increase in LFE rate during times of tidally induced compression is inconsistent with models of Coulomb stress transfer as increases in normal stress should inhibit, not promote, fault slip [*Ader et al.*, 2012]. If we account for poroelastic effects, the Skempton coefficient (the ratio of the change in pore fluid pressure due to a change in applied normal stress at undrained conditions) of > 0.9 estimated by *Hawthorne and Rubin* [2010] suggests that most of the applied normal stress is buffered by corresponding increases in fluid pressure, which also does not explain the negative FNS correlation. *Perfettini et al.* [2001] studied the effect of periodic normal stress changes on a spring-block system and found that the shear stress response could exhibit a range of phase lags relative to the normal stress fluctuations depending on model parameters. It is possible that effects such as those could explain the negative normal stress correlation, but to fully understand the effects of changing normal stress on LFE occurrence will likely require incorporating periodic changes in normal stress into slow slip simulations.

The spatial distribution of tremor sensitivity to tidal shear-stress forcing (UDSS, Figure 4b) in northern Cascadia varies in a semicoherent fashion across the region with localized areas, in particular, southwestern Vancouver Island (Region A) and the southeastern Strait of Juan de Fuca/adjacent Washington state (Region B), displaying higher sensitivity than their surroundings (H. Houston, submitted manuscript, 2014). Recent studies have used various realizations of rate-and-state friction models to argue that tidal sensitivity can be interpreted as a probe of either effective stress, frictional properties or both [*Thomas et al.*, 2009, 2012; *Ader et al.*, 2012; *Hawthorne and Rubin*, 2013; *Beeler et al.*, 2013]. Following *Beeler et al.* [2013], we can employ the observations of LFE tidal modulation and a steady state, rate-dependent friction model to constrain the physical properties of the creeping fault. The friction model is

$$\tau = \tau_0 + a\sigma_e \ln\left(\frac{V_{\mathrm{REF}}}{V_L}\right) \tag{5}$$

where τ is the maximum total shear stress resistance including tidal contributions, τ_0 is shear resistance at the long-term displacement-averaged creep rate V_L, V_{REF} is the creep rate of the fault surrounding an LFE patch, σ_e is effective normal stress, and a is the friction coefficient from rock experiments. By equating the ratio of slip rates V_{REF}/V_L to $N_{\mathrm{ex}} + 1 \approx 1.3$ [*Beeler et al.*, 2013] and assuming a value for tidal stress (UDSS) amplitude $|\tau - \tau_0| = 2$ kPa, we find $a\sigma_e = 7.6$ kPa. Assuming $a = 0.04$ (extrapolation of the rate parameter a for gabbro in hydrothermal conditions [*Liu and Rice*, 2009]), yields a mean effective normal stress of σ_e of 0.2 MPa, consistent with other model estimates between 0.2 and 3 MPa of *Liu and Rice* [2007] and *Hawthorne and Rubin* [2013]. In contrast, if we assume a typical lithostatic pressure gradient and hydrostatic pore pressure, the effective normal stress at a nominal depth of 30 km is $\sigma_e = 530$ MPa, or 3 orders of magnitude larger. The low, effective normal stress implied by the analysis above is most easily explained by high pore fluid pressures near the plate boundary [*Bartlow et al.*, 2012; *Thomas et al.*, 2012; *Beeler et al.*, 2013] as supported by the independent observations of *Audet et al.* [2009].

The existence of secondary events that appear to be tidally triggered may result in underestimated effective stress values. The model used to infer effective stress above considers the influence of tides directly on the LFE asperity and indirectly via surrounding creep [*Beeler et al.*, 2013]. Within this framework, if creep is the dominant source of stress, changes in LFE rates can be interpreted as being due solely to the modulation of the main front, as secondary events have not been documented in Parkfield (either because they do not exist or because of the limited spatial resolution of the LFE data set). In Cascadia, some LFE families possess a significant fraction of events that are related to stress changes from secondary events that the *Beeler et al.* [2013] model does not consider. For this reason, the estimated effective stress likely represents a minimum bound. Models that consider only slip rate modulation may still be valid in some parts of Cascadia because (i) some highly modulated families (e.g., LFE families numbers 1, 2, 3, 68, 77, and 78) have no events that are directly associated with identifiable RTRs (see Table S3 in the supporting information), (ii) N_{ex} values do not correlate with the percentage of RTR events in each LFE family, and (iii) non-RTR populations are still weakly modulated. These observations imply that modulation of creep rate due to tidal stress and tidal triggering of secondary events are jointly responsible for the observed tidal sensitivity.

5.2. The Role of Secondary Events

Secondary events are a more important component of slow slip processes than previously thought, as up to 34% of events within a given LFE family occur as part of RTRs and our preliminary analysis does not account for small-scale secondary events close to the main front [*Ghosh et al.*, 2010; *Obara et al.*, 2012; *Rubin and Armbruster*, 2013]. *Rubin and Armbruster* [2013] estimated ~10 kPa stress drops for the main and small-scale secondary fronts. In section 3.4, we find that the average stress drop for LFEs in an RTR is ~0.8 kPa, an order of magnitude smaller. *Hawthorne and Rubin* [2013] modeled tidal stressing on a fault that obeyed a velocity-weakening to velocity-strengthening constitutive relation and found that secondary fronts arose frequently in their simulations. However, they ultimately concluded that their modeled fronts were not a realistic representation of actual secondary fronts because they do not repeatedly rupture the same section of fault as observed, and matching observed propagation speeds requires stress drops that are comparable to those of the main front, which they considered implausibly large for their adopted model. Having equal stress drops as proposed by *Rubin and Armbruster* [2013] introduces modeling problems as it implies that the small-scale secondary fronts slip much faster than the main front in order to produce the much faster propagation speeds. This seems hard to reconcile with a single-state variable friction law [*Rubin*, 2011]. In contrast, our estimate of stress drop for LFEs in an RTR is 1 order of magnitude smaller, which means that the secondary fronts should have approximately the same slip velocity as the main front, eliminating the latter discrepancy.

The time and length scales of our RTRs and the secondary events of *Rubin and Armbruster* [2013] are different. For example, the difference in stress drop estimates arises primarily from contrasting estimates for the width of the slip front L_s (1 km versus 10 km) in (4). The temporal distinction between small-scale events and RTRs is evident in Figure 9b, which displays LFEs in green that participated in the small-scale secondary events of 3 March 2003 as reported by *Rubin and Armbruster* [2013]. We note that the succession of small-scale secondary events immediately follows the main RTR on that date, extends through a second RTR on 4 March 2003, and affects a different region closer to the main front. Similar observations hold for 14 July 2004 [see *Rubin and Armbruster*, 2013, Figures 5 and 8]. Furthermore, the small-scale events propagate at higher speeds, up to 20 km/h, than the RTRs with speeds near 5 km/h, an observation consistent with those of *Obara et al.* [2012].

Our results suggest that tides trigger RTR secondary events, but the specific role of tides in nucleating secondary events is still unclear. *Thomas et al.* [2013] showed that 12 secondary events (five RTRs and seven streaks) during the 2010 and 2011 tremor episodes occur exclusively during thrust-encouraging shear stress. Similarly, we find that 46 out of 64 RTRs occur during times of positive UDSS and have N_{ex} values that are systematically larger than non-RTR events (though we note that N_{ex} may not be an appropriate measure to quantify tidal sensitivity of RTRs). *Rubin and Armbruster* [2013] remark that their small-scale events occur throughout the tidal cycle and repeatedly rupture the same fault region, suggesting that tides alone are not a sufficient source of stress to drive small-scale secondary events. In the simulations of *Hawthorne and Rubin* [2013], large-scale secondary events result from stress recovery following the main front, tidal loading, and spatial variability in slip rate modulation due to the tides. They also found that secondary events rarely arose in simulations that did not incorporate tidal stressing.

5.3. Tidal Sensitivity and LFE Recurrence Intervals

Motivated by the observations of variable spatial sensitivity to tidal forcing, we analyze the cumulative temporal distribution of a selection of SVI LFE families at updip and downdip locations over the period 23 February 2003 through 1 July 2006 to establish whether families with different tidal sensitivities might also display distinct recurrence characteristics [*Wech and Creager*, 2011]. As in the latter study, the results in Figure 11 reveal that updip families (#18: low sensitivity—$N_{ex} = 5.1\%$, #55: high sensitivity—$N_{ex} = 36.8\%$) are characterized by large, punctuated increases in detections, principally during major ETS episodes, whereas downdip families (#16: low sensitivity—$N_{ex} = 1.9\%$, #7: high sensitivity—$N_{ex} = 24.8\%$) display a more continuous accumulation of detections, independent of tidal sensitivity. We note that LFE family #16 displays a more continuous accumulation of detections over the period 23 February 2003 through 31 August 2005 but experienced a large, punctuated increase in detections during and immediately following the 2005 ETS episode. We further note that updip, highly modulated families in SVI possess a higher percentage of RTR events (>20%). In contrast, some downdip families that have few or no RTRs also have high N_{ex} values, indicating that tidal modulation is not only due to RTRs.

Unlike previous reports from Parkfield and Shikoku, there does not appear to be a systematic variation in tremor sensitivity with depth. On the San Andreas fault near Parkfield, deeper LFE families tend to be more sensitive to tidally induced right-lateral shear stress than shallow ones [*Thomas et al.*, 2012], whereas in

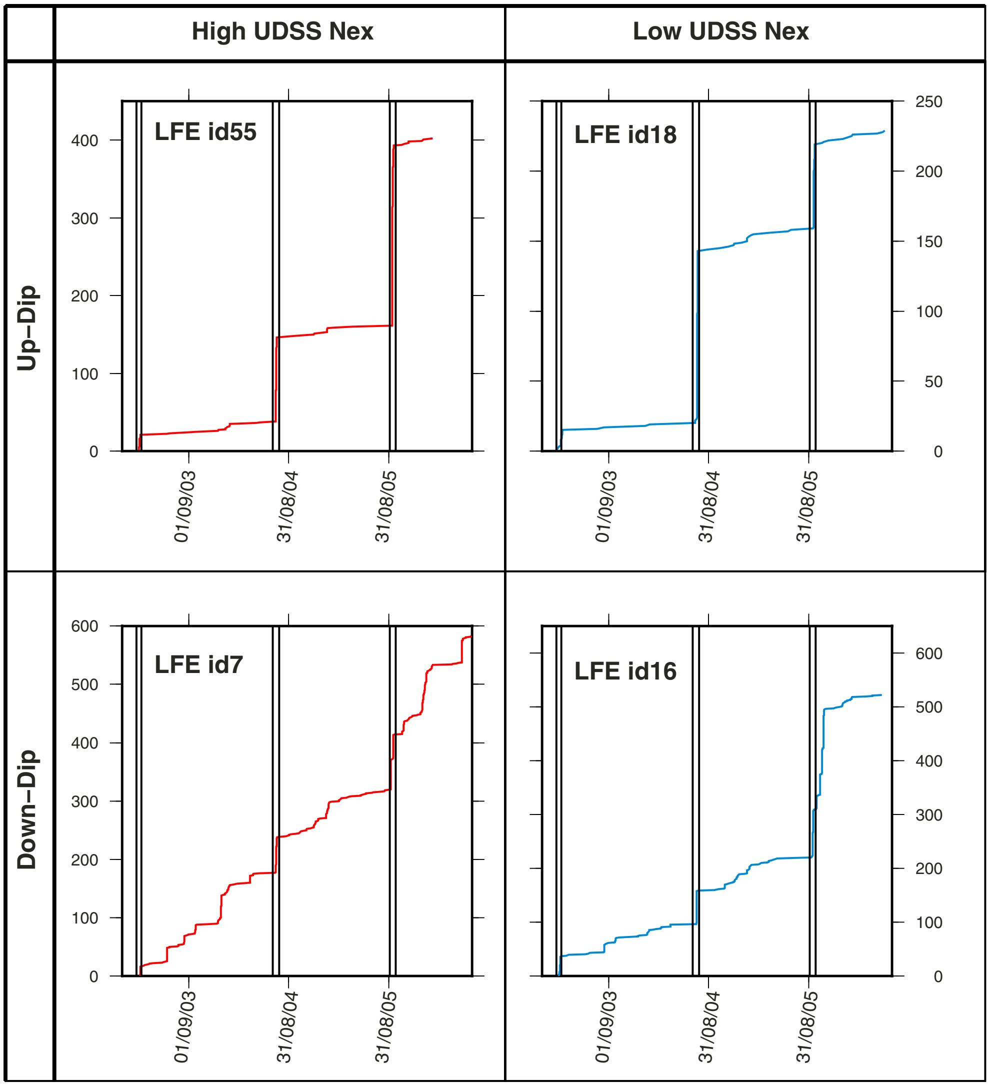

Figure 11. Cumulative distribution functions over a 3.5 year period for a selection of distinct low versus high tidal sensitivity and updip versus downdip SVI LFE families. In each plot, the ordinate axis corresponds to cumulative detections and vertical black lines demarcate major ETS episodes.

Shikoku, the highest sensitivity to tidal shear stress occurs preferentially in updip regions of tremor [*Ide*, 2010]. In contrast, our results suggest that tidal sensitivity must depend, at least in part, on physical properties that vary independently of depth, consistent with more general observations of laterally heterogeneous tremor distribution and strength [*Husker et al.*, 2012; *Gomberg and Prejean*, 2013]. In a study of tremor strength in northern Washington, using beamforming of Array-of-Arrays data between 2009 and 2010, *Ghosh et al.* [2010] isolated several patches of elevated tremor density that coincide closely in location with LFE families from our NW catalog (i.e., "region B") exhibiting strong tidal sensitivity.

5.4. Evolution of N_{ex} and Phase Shift Throughout Slow Slip Events

In sections 4.1 and 4.2 we reported time-dependent changes in both the tidal sensitivity and phase shift of LFE families throughout SSEs. Figure 7 demonstrates that LFE sensitivity to UDSS on SVI rises dramatically from near zero in the first day of strong activity to a maximum ~4 days later (~6 days later for NW). Figure 8 shows no correlation between the phase of peak LFE rate relative to peak tidal stress the first day of the SSE. However, as the SSE progresses, peak LFE rate first corresponds to peak tidal shear stress rate (dUDSS) over the second day and gradually transitions to correlation with peak tidal shear stress (UDSS) over subsequent days. A number of authors have suggested that tidal sensitivity may change relative to the background slip rate [*Lambert et al.*, 2009; *Thomas et al.*, 2012; *Hawthorne and Rubin*, 2013]. If we interpret the evolution of N_{ex} and phase as occurring primarily in response to changes in slip rate throughout the SSE, we can qualitatively compare our observations with the predictions made by three modeling studies [*Hawthorne and Rubin*, 2013; *Ader et al.*, 2012; *Beeler et al.*, 2013] that consider tidal stresses acting on SSEs within a rate-and-state friction framework. In the first two models, the change in LFE rate is interpreted as the fractional change in slip rate due to the applied tidal stress or $N_{ex} \approx \Delta V/V_{REF}$, where V_{REF} is the background slip rate. The final model incorporates stress changes on the LFE asperity from both the direct tidal stress and the surrounding creep and $N_{ex} + 1 \approx \dot{\tau}/\dot{\tau}_b$.

Ader et al. [2012] modeled modulation of slip rate due to tidal stress using a spring slider system obeying velocity-strengthening friction. After linearizing around steady state, they find expressions for both the fractional change in velocity due to an applied tidal Coulomb stress change as well as the expected phase of the peak LFE rate with respect to the phase of the Coulomb stress change. The resulting expressions predict both phase lags and advances depending on the period of tidal forcing relative to the timescales for state evolution and the timescale at which frictional damping becomes important. If the period T is similar to the timescale for state evolution T_θ, the model predicts a phase lag, whereas if the period is similar to the timescale at which frictional damping becomes unimportant, it can produce a phase advance. Using their adopted parameter values of characteristic length $D_c = 0.2$ mm, reference slip rate values between 1 and 1000 times the background plate rate of 2 cm/yr and the $T = 12.4$ h yields values of T/T_θ between 0.01 and 10, suggesting that the peak LFE rate should be in phase with the peak Coulomb stress or at a slight lag. If all other parameters are held constant, this model predicts that the modulation increases with increasing slip velocity contrary to the relationship between slip rate and modulation shown in Figure 7. Additionally, the peak LFE rate should be in phase with peak tidal stress or at a slight lag leaving the families that occur in advance of the peak slip rate unexplained. Since D_c can vary over multiple orders of magnitude [*Paterson and Wong*, 2005], appealing to spatial variability may allow the model to reproduce the observations in Figure 8.

Hawthorne and Rubin [2013] modeled slow slip and tidal stressing using a velocity-weakening to velocity-strengthening constitutive equation and found that the majority of slip and modulation occurs behind the main slip front in a region where the fault is slipping very near steady state. This model predicts greater modulation at lower slip rates because the acceleration depends on the background slip velocity; the same tidal shear stress change applied to an SSE with lower background slip velocity will result in a larger velocity increase than when applied to a family with higher-background slip velocity. This behavior is a consequence of the steady state velocity profile for this particular constitutive framework (shown in their Figure 4a) and is consistent with the observations in Figure 7. However, because increases in velocity are in response to an applied tidal stress, this particular model cannot produce peak slip rates prior to peak tidal stress shown in Figure 8.

Beeler et al. [2013] developed an asperity model to explain tidal triggering of LFEs in which LFE patches fail at a threshold stress. This model differs from the previous two in that $N_{ex} + 1 \approx \dot{\tau}/\dot{\tau}_b$, where $\dot{\tau}$ is the stressing rate on the patch and $\dot{\tau}_b$ is the background patch stressing rate. *Beeler et al.* [2013] considered three sources of stress: tectonic loading, fault creep, and direct stressing from the tides. There are a couple of ways to produce phase shifts using their model. First, the tidal stress acts both directly on the LFE patch and to modulate the surrounding creep. The former contribution is in phase with peak stressing rate, while the latter contribution depends on the specific rheology chosen for the fault surface surrounding the LFE asperity. As such, phase shifts can be achieved by balancing these two contributions through the patch stiffness. Though it may be possible for the size of individual LFE asperities to change throughout a slow slip event, we dismiss this mechanism because observational evidence for this behavior is lacking. Second, for a fixed patch size, the contribution of the surrounding creep is a function of the parameters in the constitutive equation that characterizes the surrounding fault slip. Modifying those parameters changes the relative contribution of the direct tidal stressing and surrounding creep and can produce a phase shift between peak tidal stress and peak stressing rate. Matching the phase shift observations in Figure 8 using a fixed patch size requires that the dominant source of stress be creep at low slip rates and direct tidal stressing at high slip rates. If we simply assume that the surrounding fault obeys velocity-strengthening friction, this model can reproduce the relationship between slip rate and tidal sensitivity; however, since the contribution from creep increases with increasing V_{REF}, it cannot reproduce the observed phase relationship if all other parameters are held constant.

Finally, we remark that all of the models discussed above consider tidal sensitivity of LFEs to be due to the modulation of the slip rate by the applied tidal stress and ignore the role of triggering. *Thomas et al.* [2013] recently demonstrated that large-scale secondary fronts in Cascadia are tidally triggered. We also observe that a majority of RTRs occur during the time of positive UDSS, and associated N_{ex} are always higher than the N_{ex} of non-RTR events. It is worthwhile to note that, as shown in Figure 9b, RTRs start a few days after the first day of strong activity and therefore RTRs probably play a role in the observed increase of tidal sensitivity with time. If a large fraction of LFEs within a given slip episode occur as part of secondary fronts then the models discussed above may be only partially valid.

5.5. Twenty-Four Hour Periodicity of LFE Detections

The presence of a 24 h periodicity in tremor occurrence in northern Cascadia previously documented by *Rubinstein et al.* [2008], *Wech and Creager* [2008], and *Lambert et al.* [2009] is clearly evident within the LFE catalogs as a deficit of detections between 6 A.M. and 3 P.M. (Pacific Daylight Savings Time) through the entire area of study (see Figure 10). We also note a “weekend” effect with an increase in detections during working hours of weekend days, as observed in Wech’s tremor catalog (A. G. Wech, personal communication, 2014). The correspondence of this time interval with regular working hours suggests that anthropogenic cultural noise contributes to increased detection thresholds during working hours [e.g., *Rydelek and Sacks*, 1989] and that a larger proportion of events are undetected during the half cycle of working hours. Given the time frame of our LFE detections (e.g., 10 three week ETS episodes recorded over 11 years for SVI), we believe that any biassing effects on our tidal analysis due to diurnal variations are minimal.

6. Conclusions

We analyzed the sensitivity of LFEs to tidal forces using three LFE detection catalogs for northern Cascadia. We find localized areas showing higher sensitivity to UDSS than their surroundings, which suggests that tidal sensitivity must partially depend on laterally heterogeneous physical properties such as variable pore fluid pressures and frictional properties along the plate interface. The majority of LFEs in southern Vancouver Island and northern Washington fail during times of large, positive, and increasing UDSS. There also appears to be a significant, yet more ambiguous, contribution from normal stress changes.

For seven tremor episodes in southern Vancouver Island, we identified 64 RTRs with a characteristic duration of ∼4 h and a mean velocity of ∼5 km/h. Secondary events are an important component of slow slip processes as up to one third of events within a given LFE family occur as part of RTRs. A majority of RTRs occur during periods of positive UDSS, with N_{ex} values larger than non-RTR events, suggesting that tides may trigger secondary events. Therefore, the observed tidal sensitivity to UDSS likely represents a combination of modulation of creep rate due to tidal stress and tidal triggering of secondary events. The average stress drop for LFEs in a RTR is estimated to be ∼0.8 kPa, 1 order of magnitude smaller than the estimated stress drop of the main slip front and small-scale secondary fronts estimated by *Rubin and Armbruster* [2013].

We find that sensitivity to UDSS rises dramatically from near zero in the first day of strong activity to a maximum 4 days later. In addition, the phase of the peak LFE rate transitions from being in phase with the peak tidal shear stress rate to being in phase with peak tidal shear stress. We qualitatively compared the observations to three proposed modeling frameworks. If we assume that the slip rate is primarily responsible for the changes in tidal sensitivity and phase (i.e., parameters other than the slow slip rate are held constant) then we find that none of the proposed frameworks can reproduce both the sensitivity and phase observations. We suspect that RTRs are also partly responsible for the increase of tidal sensitivity with time as RTRs start few days after the beginning of strong activity and display high UDSS N_{ex}.

The presence of a 24 h periodicity in tremor occurrence in northern Cascadia suggests that anthropogenic cultural noise contributes to increased detection thresholds during working hours and that a larger proportion of detections is missed during the half cycle of working hours.

Acknowledgments
We gratefully acknowledge the helpful comments of Nick Beeler, Roland Burgmann, Jessica Hawthorne, Allan Rubin, and David Shelly on a preliminary draft of the manuscript. We acknowledge constructive reviews from the Associate Editor and referees and, in particular, Heidi Houston for her suggestion that we investigate temporal sensitivity of tidal phase. This research was supported by NSERC grant RGPIN 138004 to M.G.B. and NSF grant 1249775 to A.M.T. Waveform data used in this study are freely available from the Canadian National Seismograph Network and the Incorporated Research Institutions for Seismology data centers. Data processed from these waveforms are available by request from Michael Bostock at bostock@eos.ubc.ca.

References

Ader, T. J., J.-P. Ampuero, and J.-P. Avouac (2012), The role of velocity-neutral creep on the modulation of tectonic tremor activity by periodic loading, *Geophys. Res. Lett.*, *39*, L16310, doi:10.1029/2012GL052326.

Agnew, D. C. (2012), SPOTL: Some programs for ocean tide loading, *SIO Tech. Rep. Scripps Inst. Oceanogr.*, Univ. of Calif., La Jolla.

Audet, P., M. G. Bostock, N. I. Christensen, and S. M. Peacock (2009), Seismic evidence for overpressured subducted oceanic crust and megathrust fault sealing, *Nature*, *457*, 76–78, doi:10.1038/nature07650.

Audet, P., M. G. Bostock, D. C. Boyarko, M. R. Brudzinski, and R. M. Allen (2010), Slab morphology in the Cascadia fore arc and its relation to episodic tremor and slip, *J. Geophys. Res.*, *115*, B00A16, doi:10.1029/2008JB006053.

Bartlow, N. M., D. A. Lockner, and N. M. Beeler (2012), Laboratory triggering of stick-slip events by oscillatory loading in the presence of pore fluid with implications for physics of tectonic tremor, *J. Geophys. Res.*, *117*, B11411, doi:10.1029/2012JB009452.

Beeler, N. M., A. M. Thomas, R. Bürgmann, and D. R. Shelly (2013), Inferring fault rheology from low-frequency earthquakes on the San Andreas, *J. Geophys. Res. Solid Earth*, *118*, 5976–5990, doi:10.1002/2013JB010118.

Bostock, M. G., A. A. Royer, E. H. Hearn, and S. M. Peacock (2012), Low frequency earthquakes below southern Vancouver Island, *Geochem. Geophys. Geosyst.*, *13*, Q11007, doi:10.1029/2012GC004391.

Egbert, G. D., A. F. Bennet, and M. G. G. Foreman (1994), TOPEX/POSEIDON tides estimated using a global inverse model, *J. Geophys. Res.*, *99*, 24,821–24,852, doi:10.1029/94JC01894.

Farrell, W. E. (1972), Deformation of the Earth by surface loads, *Rev. Geophys.*, *10*(3), 761–797, doi:10.1029/RG010i003p00761.

Gallego, A., R. M. Russo, D. Comte, V. Mocanu, R. E. Murdie, and J. C. VanDecar (2013), Tidal modulation of continuous nonvolcanic seismic tremor in the Chile triple junction region, *Geochem. Geophys. Geosyst.*, *14*, 851–863, doi:10.1002/ggge.20091.

Ghosh, A., J. E. Vidale, and K. C. Creager (2010), Tremor asperities in the transition zone control evolution of slow earthquakes, *J. Geophys. Res.*, *117*, B10301, doi:10.1029/2010GL043723.

Ghosh, A., J. E. Vidale, J. R. Sweet, K. C. Creager, A. G. Wech, H. Houston, and E. E. Brodsky (2010), Rapid, continuous streaking of tremor in Cascadia, *Geochem. Geophys. Geosyst.*, *11*, Q12010, doi:10.1029/2010GC003305.

Gomberg, J., and S. Prejean (2013), Triggered tremor sweet spots in Alaska, *J. Geophys. Res. Solid Earth*, *118*, 6203–6218, doi:10.1002/2013JB010273.

Hawthorne, J. C., and A. M. Rubin (2010), Tidal modulation of slow slip in Cascadia, *J. Geophys. Res.*, *115*, B09406, doi:10.1029/2010JB007502.

Hawthorne, J. C., and A. M. Rubin (2013), Tidal modulation and back-propagating fronts in slow slip events simulated with a velocity-weakening to velocity-strenghtening friction law, *J. Geophys. Res. Solid Earth*, *118*, 1216–1239, doi:10.1002/jgrb.50107.

Houston, H. (2013), ETS and tidal stressing: Fault weakening after the main slip pulse, Abstract S51D-02 presented at 2013 Fall Meeting, AGU, San Francisco, Calif. 9-13 Dec.

Houston, H., B. G. Delbridge, A. G. Wech, and K. C. Creager (2011), Rapid tremor reversals in Cascadia generated by a weakened plate interface, *Nat. Geosci.*, *4*, 404–409, doi:10.1038/ngeo1157.

Husker, A. L., V. M. Cruz-Atienza, D. Legrand, N. M. Shapiro, J. S. Payero, M. Campillo, and E. Huesca-Pérez (2012), Temporal variations of non-volcanic tremor (NVT) locations in the Mexican subduction zone: Finding the NVT sweet spot, *Geochem. Geophys. Geosyst.*, *13*, Q03011, doi:10.1029/2011GC003916.

Ide, S. (2010), Striations, duration, migration and tidal response in deep tremor, *Nature*, *466*(7304), 356–359, doi:10.1038/nature09251.

Ide, S., and Y. Tanaka (2014), Controls on plate motion by oscillating tidal stress: Evidence from deep tremors in western Japan, *Geophys. Res. Lett.*, *41*, 3842–3850, doi:10.1002/2014GL060035.

Klaus, A. (2012), Modulation of Cascadia tremor amplitude by tidal stresses, MSc thesis, Univ. of Washington, Seattle.

Lambert, A., H. Kao, G. Rogers, and N. Courtier (2009), Correlation of tremor activity with tidal stress in the northern Cascadia subduction zone, *J. Geophys. Res.*, *114*, B00A08, doi:10.1029/2008JB006038.

Liu, Y., and J. R. Rice (2007), Spontaneous and triggered aseismic deformation transients in a subduction fault model, *J. Geophys. Res.*, *112*, B09404, doi:10.1029/2007JB004930.

Liu, Y., and J. R. Rice (2009), Slow slip predictions based on granite and gabbro friction data compared to GPS measurements in northern Cascadia, *J. Geophys. Res.*, *114*, B09407, doi:10.1029/2008JB006142.

McCrory, P. A., J. L. Blair, F. Waldhauser, and D. H. Oppenheimer (2012), Juan de Fuca slab geometry and its relation to Wadati-Benioff zone seismicity, *J. Geophys. Res.*, *117*, B09306, doi:10.1029/2012JB009407.

Melchior, P. (1978), *The Tides of the Planet Earth*, Pergamon, Oxford, U. K.

Miyazawa, M., and J. Mori (2005), Detection of triggered deep low-frequency events from the 2003 Tokachi-oki earthquake, *Geophys. Res. Lett.*, *32*, L10307, doi:10.1029/2005GL022539.

Nakata, R., N. Suda, and H. Tsuruoka (2008), Non-volcanic tremor resulting from the combined effect of Earth tides and slow slip events, *Nat. Geosci.*, *1*, 676–678, doi:10.1016/j.tecto.2005.09.013.

Obara, K., T. Matsuzawa, S. Tanaka, and T. Maeda (2012), Depth-dependent mode of tremor migration beneath Kii Peninsula, Nankai subduction zone, *Geophys. Res. Lett.*, *39*, L10308, doi:10.1029/2012GL051420.

Paterson, M. S., and T.-F. Wong (2005), *Experimental Rock Deformation—The Brittle Field*, 2nd ed., 347 pp., Springer, New York.

Peng, Z., and K. Chao (2008), Non-volcanic tremor beneath the Central Range in Tawain triggered by the 2001 M_w 7.8 Kunlun earthquake, *Geophys. J. Int.*, *175*, 825–829, doi:10.1111/j.1365-246X.2008.03886.x.

Peng, Z., J. E. Vidale, K. C. Creager, J. L. Rubinstein, J. Gomberg, and P. Bodin (2008), Strong tremor near Parkfield, CA, excited by the 2002 Denali Fault earthquake, *Geophys. Res. Lett.*, *35*, L23305, doi:10.1029/ 2008GL036080.

Perfettini, H., J. Schmittbuhl, J. R. Rice, and M. Cocco (2001), Frictional response induced by time-dependent fluctuations of the normal loading, *J. Geophys. Res.*, *106*(B7), 13,455–13,472, doi:10.1029/2000JB900366.

Royer, A. A., and M. G. Bostock (2013), A comparative study of low frequency earthquake templates in northern Cascadia, *Earth Planet. Sci. Lett.*, *402*, 247–256, doi:10.1016/j.epsl.2013.08.040.

Rubin, A. M. (2011), Designer friction laws for bimodal slow slip propagation speeds, *Geochem. Geophys. Geosyst.*, *12*, Q04007, doi:10.1029/2010GC003386.

Rubin, A. M., and J. G. Armbruster (2013), Imaging slow slip fronts in Cascadia with high precision cross-station tremor locations, *Geochem. Geophys. Geosyst.*, *14*, 5371–5392, doi:10.1002/2013GC005031.

Rubinstein, J. L., J. E. Vidale, J. Gomberg, P. Bodin, K. C. Creager, and S. D. Malone (2007), Non-volcanic tremor driven by large transient shear stresses, *Nature*, *448*, 579–582, doi:10.1038/nature06017.

Rubinstein, J. L., M. L. Rocca, J. E. Vidale, K. C. Creager, and A. G. Wech (2008), Tidal modulation of nonvolcanic tremor, *Science*, *319*, 186–189, doi:10.1126/science.1150558.

Rubinstein, J. L., J. Gomberg, J. E. Vidale, A. G. Wech, H. Kao, K. C. Creager, and G. Rogers (2009), Seismic wave triggering of nonvolcanic tremor, episodic tremor and slip, and earthquakes on Vancouver Island, *J. Geophys. Res.*, *114*, B00A01, doi:10.1029/2008JB005875.

Rydelek, P. A., and I. S. Sacks (1989), Testing the completeness of earthquake catalogues and the hypothesis of self-similarity, *Nature*, *337*, 251–253, doi:10.1038/337251a0.

Schmidt, D. A., and H. Gao (2010), Source parameters and time-dependent slip distributions of slow slip events on the Cascadia subduction zone from 1998 to 2008, *J. Geophys. Res.*, *115*, doi:10.1029/2008JB006045.

Shelly, D. R., G. C. Beroza, and S. Ide (2007a), Complex evolution of transient slip derived from precise tremor locations in western Shikoku, Japan, *Geochem. Geophys. Geosyst.*, *8*, Q10014, doi:10.1029/2007GC001640.

Shelly, D. R., G. C. Beroza, S. Ide, and S. Nakamula (2007b), Low frequency earthquakes in Shikoku, Japan, and their relationship to episodic tremor and slip, *Nature*, *442*, 188–191, doi:10.1038/nature04931.

Szeliga, W., T. I. Melbourne, M. Santillan, and M. Miller (2008), GPS constraints on 34 slow slip events within the Cascadia subduction zone, 1997–2005, *J. Geophys. Res.*, *113*, B04404, doi:10.1029/2007JB004948.

Tanaka, S., M. Ohtake, and H. Sato (2002), Evidence for tidal triggering of earthquakes as revealed from statistical analysis of global data, *J. Geophys. Res.*, *107*(B10), 2211, doi:10.1029/2001JB001577.

Thomas, A. M., R. M. Nadeau, and R. Burgmann (2009), Tremor-tide correlations and near-lithostatic pore pressure on the deep San Andreas fault, *Nature*, *462*, 1048–1051, doi:10.1038/nature08654.

Thomas, A. M., R. Bürgmann, D. R. Shelly, N. M. Beeler, and M. L. Rudolph (2012), Tidal triggering of low-frequency earthquakes near Parkfield, California: Implications for fault mechanics within the brittle-ductile transition, *J. Geophys. Res.*, *117*, B05301, doi:10.1029/2011JB009036.

Thomas, T. W., J. E. Vidale, H. Houston, K. C. Creager, J. R. Sweet, and A. Ghosh (2013), Evidence for tidal triggering of high-amplitude rapid tremor reversals and tremor streaks in northern Cascadia, *Geophys. Res. Lett.*, *40*, 4254–4259, doi:10.1002/grl.50832.

Wech, A. G., and K. C. Creager (2008), Automated detection and location of Cascadia tremor, *Geochem. Geophys. Geosyst.*, *35*, L20302, doi:10.1029/2008GL035458.

Wech, A. G., and K. C. Creager (2011), A continuum of stress, strength and slip in the Cascadia subduction zone, *Nat. Geosci.*, *4*, 624–628, doi:10.1038/ngeo1215.

Wech, A. G., K. C. Creager, and T. I. Melbourne (2009), Seismic and geodetic constraints on Cascadia slow slip, *J. Geophys. Res.*, *114*, B10316, doi:10.1029/2008JB006090.